6/7/2025 3:34:04 PM

## Compare Results

Old File:

ISARA\_Manuscript\_R0.pdf

**41 pages (5.38 MB)** 6/7/2025 7:32:02 PM

versus

New File:

ISARA\_Manuscript\_R1.pdf

**49 pages (5.78 MB)** 6/7/2025 6:54:05 PM

**Total Changes** 

Content

2849<sup>631</sup><sub>881</sub>

Replacements

Insertions

60 Deletions

Styling and Annotations

180 Styling

697 Annotations

Go to First Change (page 1)

# Closing the Gap: An Algorithmic Approach to Reconciling In-Situ and Remotely Sensed Aerosol Particle Properties

Sanja Dmitrovic<sup>1,\*</sup>, Joseph S. Schlosser<sup>2,3,\*</sup>, Ryan Bennett<sup>4</sup>, Brian Cairns<sup>5</sup>, Gao Chen<sup>2</sup>, Glenn S. Diskin<sup>2</sup>, Richard A. Ferrare<sup>2</sup>, Johnathan W. Hair<sup>2</sup>, Michael A. Jones<sup>6</sup>, Jeffrey S. Reid<sup>7</sup>, Taylor J. Shingler<sup>2</sup>, Michael A. Shook<sup>2</sup>, Armin Sorooshian<sup>1,8,9</sup>, Kenneth L. Thornhill<sup>2,10</sup>, Luke D. Ziemba<sup>2</sup>, and Snorre Stamnes<sup>2</sup>

Correspondence to: Joseph S. Schlosser (joseph.s.schlosser@nasa.gov)

**Abstract.** Remote sensing retrievals of atmospheric aerosol particle properties, such as those from lidars and polarimeters, are increasingly used to study aerosol impacts on critical cloud and marine boundary layer processes. To ensure the reliability of these retrievals, it is important to validate them using aerosol measurements from in-situ instruments (i.e., external closure). However, achieving rigorous external closure is challenging because in-situ instruments often 1) provide dry (relative humidity (RH) < 40%) aerosol measurements, while remote sensors typically retrieve properties in ambient conditions and 2) only sample a limited aerosol particle size range due to sampling inlet cutoffs. To address these challenges, we introduce the In-Situ Aerosol Retrieval Algorithm (ISARA), a software framework designed to enable closure between in-situ and remote sensing aerosol data by converting dry in-situ aerosol optical and microphysical properties into ambient, humidified ones. We apply ISARA to aerosol measurements collected during the NASA Aerosol Cloud meTeorology Interactions oVer the western ATlantic Experiment (ACTIVATE) field campaign to test its ability to generate aerosol properties that are comparable across measurement platforms. To assess this performance, we conduct consistency analysis by comparing ISARA-calculated aerosol data with corresponding measurements from 1) ACTIVATE's in-situ instruments (internal consistency), 2) Monte Carlo in-situ data simulations (synthetic consistency), and 3) ACTIVATE's Second Generation High Spectral Resolution Lidar (HSRL-2) and Research Scanning Polarimeter (RSP) instruments (external consistency). This study demonstrates that: 1) appropriate a priori assumptions for aerosol particles can lead to consistency between many in-situ measurements and remote sensing retrievals in the ACTIVATE campaign, 2) ambient aerosol properties retrieved from dry in-situ and the RSP polarimetric data are shown to be consistent for the first time in literature, 3) measurements are externally consistent even in the presence of

<sup>&</sup>lt;sup>1</sup>University of Arizona, James C. Wyant College of Optical Sciences, Tucson, Arizona, USA

<sup>&</sup>lt;sup>2</sup>NASA Langley Research Center, Hampton, Virginia, USA

<sup>&</sup>lt;sup>3</sup>NASA Postdoctoral Program, NASA Langley Research Center, Hampton, Virginia, USA

<sup>&</sup>lt;sup>4</sup>Bay Area Environmental Research Institute, Ventura, California, USA

<sup>&</sup>lt;sup>5</sup>NASA Goddard Institute for Space Studies, New York, New York, USA

<sup>&</sup>lt;sup>6</sup>University of Massachusetts Lowell, Lowell Center for Space Science and Technology, Lowell, Massachusetts, USA

<sup>&</sup>lt;sup>7</sup>U.S. Naval Research Laboratory, Marine Meteorology Division, Monterey, California, USA

<sup>&</sup>lt;sup>8</sup>University of Arizona, Department of Chemical and Environmental Engineering, Tucson, Arizona, USA

<sup>&</sup>lt;sup>9</sup>University of Arizona, Department of Hydrology and Atmospheric Sciences, Tucson, Arizona, USA

<sup>&</sup>lt;sup>10</sup>Analytical Mechanics Associates, Hampton, Virginia, USA

<sup>\*</sup>These authors contributed equally to this work.

moderately absorbing (imaginary refractive index (IRI) > 0.015) aerosol, and 4) ISARA is limited by probable under-sampling of coarse-mode particles as well as by an under-determined system. While this study focuses on spherical, sulfate-dominated aerosol mixtures, its overall success demonstrates that ISARA has the potential to support systematic and streamlined closure of aerosol datasets across diverse field campaigns and aerosol regimes.

#### 1 Introduction

40

Atmospheric aerosol particles play a central role in Earth's climate system by scattering and absorbing solar radiation (direct effect) and by serving as cloud condensation nuclei (CCN) that influence cloud formation and radiative properties (indirect effect). Given their central role in regulating Earth's radiation balance and cloud development, aerosol particles are the target of intensive observational efforts using ground-based, airborne, and satellite instruments. These platforms are designed to measure or retrieve key aerosol optical and microphysical properties involved in these critical atmospheric processes. Because designs and error characteristics vary widely across instrument platforms, it is important to verify that aerosol measurements from one platform are consistent with those from another (i.e., external closure), as these observations are used to constrain global climate models that simulate aerosol-cloud interactions and climate feedbacks. While external closure addresses technical consistency between neasurements, it also advances aerosol science by enabling efforts to 1) validate the accuracy and uncertainty of satellite and airborne remote sensing aerosol products, 2) create improved a priori aerosol particle properties to better constrain satellite retrievals, 3) aid atmospheric modeling efforts by establishing new applications for remote sensing products such as deriving parameterizations of aerosol hygroscopi@QQQQ(4) advance the methods used to derive ambient aerosol properties from in-situ measurements. This paper aims to address these critical needs in aerosol science by assessing consistency between in-situ and remotely-sensed aerosol properties using data collected from two state-of-the-art remote sensing instruments; the Second Generation High Spectral Resolution Lidar (HSRL-2) and the Research Scanning Polarimeter (RSP). The HSRL-2 and RSP provide vertically resolved and column retrievals, respectively, of aerosol optical and microphysical properties, among other products. Details on these instruments will be provided in Sect. 2.3.

There have been numerous past efforts on assessing consistency between aerosol data sets obtained from airborne in-situ and NASA's HSRL-2 and RSP instruments. For example, more recent works have attempted to demonstrate the consistency of airborne HSRL-2 extinction and backscatter measurements and HSRL-2-retrieved aerosol effective radiususing collocated in-situ aerosol products (e.g., Müller et al., 2014; Sawamura et al., 2017; Tsekeri et al., 2017; Pistone et al., 2019). These studies consistently find that the extinction and backscatter coefficients derived from in-situ instruments are systematically low compared to those derived from HSRL-2. Additionally, evaluations of RSP retrievals of aerosol optical and microphysical properties have been performed using data from the AErosol RObotic NETwork (AERONET) (e.g., Wust al., 2015; Fu et al., 2020). There have also been a limited number of case studies successfully making comparisons between RSP retrievals and airborne in-situ data from the Arctic Research of the Composition of the Troposphere from Aircraft and Satellites (ARCTAS; Knobelspiesse et al., 2011) and ObseRvations of Aerosols above CLouds and their intEractionS (ORACLES; Pistone et al.)

2019) field campaigns. In particular, Pistone et al. (2019) found poor agreement between in-situ- and RSP- derived total SSA. However, total, fine-mode, and coarse-mode aerosol microphysical properties from RSP have not been systematically evaluated against in-situ aerosol data as of the date of this study.

Despite the important findings from these studies, a framework for systematic and streamlined closure of remote sensing aerosol data sets has not been yet achieved. Closure is challenging to perform due to the increasing volume and complexity of remote sensing data. Also, in-situ aerosol data sets can be affected by errors resulting from factors such as plumbing losses, calibration issues, and most importantly, the alteration of the aerosol's relative humidity (RH) while sampling through aircraft inlets. In order to avoid the complexities of RH variation, in-situ instruments will often dry the critical optical property and size distribution measurements of aerosol particles to RH \leq 40\%. Note that 40\% RH is the minimum efflorescence point of the majority of atmospheric aerosol species (Li et al., 2014). This drying process is often achieved using a Nafion dryer or heating in the sampling line (Sorooshian et al., 2023).

Unlike the controlled environments of many in-situ instruments, remote sensors such as lidars and polarimeters retrieve these particles' properties without altering their RH (i.e., in ambient conditions). Although aircraft in-situ instruments can measure ambient RH and apply it to dry aerosol data sets, these measurements can have errors as high as 15% (Diskin et al., 2002). Adding to this complexity, both the parameterization and measurement of hygroscopic an also have a high uncertainty (Shingler et al., 2016; Petters and Kreidenweis, 2007). Aerosol particle hygroscopicity is commonly defined as the increase in particle diameter, relative to the dry state that is due to atmospheric moisture and is typically parameterized by the physical hygroscopicity parameterization is indirectly related to changes in scattering coefficients, based on assumptions on particle shape. Alternatively, hygroscopicity can also be parameterized directly based on the increase in scattering coefficients of particles due to hygroscopic growth, referred to as the optical hygroscopicity parameter ( $\gamma$ ; Sawamura et al., 2017). These parameterizations are discussed in more detail in Section 2.4.

These sources of error can therefore significantly alter the measured or derived microphysical and optical characteristics of aerosol particles. The other major difficulty of closure is that in-situ instruments cannot efficiently sample coarse-mode particles due to limitations in the inlet cutoff diameter (i.e., typical cutoff particle diameter (D) < 5  $\mu$ m). Wing mounted probes are commonly used to estimate coarse mode aerosol properties, but are designed in such a way that the sizing can be highly uncertain (e.g., Reid et al., 2003, 2006). In addition to the coarse-mode sampling limitations, particles are lost between the external inlet of the aircraft and the inlets of the instruments (Baron and Willeke, 2001; Kulkarni et al., 2011).

75

To strive toward streamlined systematic closure of in-situ and remote sensing aerosol data sets within aircraft field campaigns, this study assesses the agreement between these two disparate measurement approaches, a process that is referred to as consistency or consistency analysis throughout this paper. To facilitate this comparison and eventually support broader closure

efforts across field campaigns, we introduce the In-Situ Aerosol Retrieval Algorithm (ISARA). Python-based retrieval algorithm that applies hygroscopic growth to dry in-situ aerosol and optical microphysical properties to derive ambient, humidified properties suitable for comparison with remote sensing retrievals. Specifically, the algorithm uses the Fortran-based Modeled Optical Properties of Ensembles of Aerosol Particles package (MOPSMAP; Gasteiger and Wiegner, 2018) based on measured size distributions and retrieved refractive indices derived from a "common" suite of in-situ instruments. This study builds on previous efforts such as Ziemba et al. (2013) and Sawamura et al. (2017), which developed similar algorithms for retrieving ambient aerosol properties from in-situ data. However, those studies focused on regions with limited coarse-mode aerosol and therefore assumed negligible coarse-mode contribution, restricting their analyses to fine-mode particles.

95 Note that in this study, the fine-mode particle regime is defined as aerosol particles with an ambient particle diameter range of 0.09–1.00 μm and the coarse-mode regime is defined as aerosol particles with ambient particle diameters ≥1.0 μm. Coarse-mode species such as dry sea salt and dust are difficult to consider because they can have particle diameters > 1.0 μm (Hussein et al., 2005). Also, dry sea salt is non-spherical non-absorbing, and very hygroscopic, which translates to larger values of κ (Sorribas et al., 2015; Ferrare et al., 2023). Similar to dry sea salt, dust can also be non-spherical but can be moderately absorbing and has a complex refractive index (CRI) that is dependent on wavelength (Voshchinnikov and Farafonov, 1993; Veselovskii et al., 2010; Wagner et al., 2012; Sorribas et al., 2015). This wave attempts to overcome these limitations by using wing mounted probes that sample coarse-mode to estimate the contribution of coarse-mode particles to calculated ambient optical and microphysical data, which is common for studies looking to account for coarse-mode (Ryder et al., 2015; Tsekeri et al., 2017; Ryder et al., 2018). While the current study focuses on the consistency analysis between in-situ- and remote sensing-derived aerosol properties of the more common spherical aerosol particles, it is hoped that the framework described in this study serves as an open source foundation that can be easily expanded and used to fully understand the information train between all manner of measurements and therefore enable systematic closure of field campaign aerosol data.

The ability of ISARA to perform consistency analyses is tested by applying the algorithm to synthesized data as well as data collected during the NASA Aerosol Cloud meTeorology Interactions oVer the western ATlantic Experiment (ACTIVATE) field campaign, a mission dedicated to characterizing aerosol-cloud-meteorology interactions by using two spatially-synchronized aircraft to provide systematic and simultaneous airborne measurements from 2020 to 2022 (Sorooshian et al., 2019). The spatial synchronization of these aircraft is ideal for performing a consistency analysis between in-situ, lidar, and polarimetric measurements since rigorous spatiotemporal collocation between these data sets can be achieved. The ACTIVATE data set also enables investigation of numerous atmospheric processes over the western North Atlantic Ocean, including aerosol-cloud interactions that represent the largest uncertainty in estimates of total anthropogenic radiative forcing (Field et al., 2014).

In addition to having a data set with ample amounts of collocated data, special effort was made to sample the North American anthropogenic outflow over the western North Atlantic ocean (Sorooshian et al., 2019). The fine-mode particles of this anthropogenic outflow ( $D < 1.0 \,\mu m$ ) are predominately composed of fresh or aged sulfate and organics (Dadashazar et al., 2022a),

120

and the coarse-mode particles ( $D \ge 1.0 \,\mu m$ ) are predominately composed of sea salt. While there are cases of diverse aerosol species that are sampled during ACTIVATE such as amines (Corral et al., 2022), dust (Ajayi et al., 2024), and smoke (Soloff et al., 2024), this study serves only to establish the utility of the ISARA and focuses on the less complex fine-mode spherical aerosol species, while the coarse-mode is assumed to be sea salt. This will limit the scope of this study and allow for future work to be done in analyzing consistency between the ambient aerosol particle properties derived from in-situ and remote sensing measurements of specific aerosol species. The ACTIVATE data set is discussed in more detail in Sect. 2.2.

With this background, we introduce a three-fold consistency analysis framework to evaluate the performance and robustness of the ISARA algorithm. The central goal of consistency and closure efforts is to enable one-to-one comparisons between in-situ and remote sensing data sets. While ISARA is designed to account for differences in aerosol properties due to relative humidity, challenges remain in achieving true one-to-one comparison due to the limited ability of in-situ instruments to sample coarse-mode particles and statistical uncertainties in the retrievals themselves. To assess whether ISARA produces aerosol properties that are accurate and comparable across platforms, we perform three types of consistency analysis: 1) synthetic consistency, using Monte Carlo-generated data to test retrieval accuracy under controlled conditions; 2) internal consistency, comparing ISARA-derived aerosol properties with corresponding instrument measurements; and 3) external consistency, assessing agreement between ISARA-derived properties and remote sensing retrievals from HSRL-2 and RSP.

Section 2 outlines the methodological framework, which includes: 1) ACTIVATE mission; 2) cloud filtering of in-situ data; 3) ISARA methodology including retrieval descriptions for dry CRI and  $\kappa$ ; 4) synthetic in-situ data generation; 5) HSRL-2 and RSP data processing including cloud filtering of remote sensing data and matching HSRL-2 data to the RSP resolution; and 6) collocation of in-situ data to the remote sensing data. Section 3 presents results of the synthetic, internal, and external measurement consistency analyses. The external measurement consistency analysis is conducted under ideal conditions defined as: i) good data spatiotemporal collocation (defined as a spatiotemporal separation of <6 min and <15 km) between the platforms, ii) a single observed aerosol layer dominated by spherical fine-mode particles (e.g., anthropogenic outflow), and iii) absence of clouds within remote sensing retrievals and in-situ measurements. Section 4 summarizes key points of this study and suggests potential avenues for future work.

### 2 Methods

135

140

145

#### 2.1 Background on Properties of Particles

While a comprehensive theoretical framework of particle properties is beyond the scope of this work, a brief summary to this study's closure calculations is provided. Fundamentally, a particle's properties are defined by its size, shape, and composition. Atmospheric particles can vary in shape and morphology depending on their species and history, but they are typically categorized as spherical or non-spherical to first order. Particle size is described in terms of radius or diameter, however this becomes dependent on the orientation of a particle for non-spherical particles. In cases of non-spherical particles, spherically equivalent

diameter is sometimes used. Many species of aerosol particles are closely approximated by spherical particles with the notable exceptions of dust, smoke, dry sea salt, and pollen. The composition of a particle defines the particle CRI that is a complex number that depends on the particle's composition and is defined as follows:

$$CRI = RRI + IRI \times i, \tag{1}$$

where RRI and IRI are the real and imaginary components of CRI, respectively. The IRI of a particle indicates how much incoming light it absorbs and the RRI of a particle indicates how much of the incoming light is scattered. The particle properties of size, shape, and composition physically govern how a particle scatters and absorbs incoming light. Regardless of the shape, the intrinsic optical properties of any randomly oriented particle of a given size are contained within the scattering and absorption efficiency ( $Q_{\text{scat}}$  and  $Q_{\text{abs}}$ , respectively) and the angular scattering matrix (**F**) of a particle (Mishchenko and Travis, 1998; Gasteiger and Wiegner, 2018). The **F** describes the angle and relative intensity of scattered light and is defined as follows:

160

175

$$\mathbf{F}(\theta) = \begin{bmatrix} a_1(\theta) & b_1(\theta) & 0 & 0 \\ b_1(\theta) & a_2(\theta) & 0 & 0 \\ 0 & 0 & a_3(\theta) & b_2(\theta) \\ 0 & 0 & -b_2(\theta) & a_4(\theta) \end{bmatrix},$$
(2)

where  $\theta$  is the angle of the scattered light. Within the angular scattering matrix, the first element is defined as phase function  $(a_1)$ .

So far, we have defined the intensive properties of single particles; however, measurements of aerosol properties are done with respect to a ensemble of particles. Ensembles of particles can have extrinsic properties that are dependent on the amount of particles that are present in addition to the intrinsic properties of those particles. Extrinsic particle properties include number, volume, and surface area concentration as well as extinction, absorption, scattering, and backscatter coefficients. In order to determine the intrinsic properties of in-situ measurements of an ensemble of aerosol particles, we use MOPSMAP that is capable of resolving the intrinsic and extrinsic properties of various particle shapes and sizes. For the purposes of this study, we limit our analysis to spherical particles.

Given this assumption of particle sphericity, we use Mie theory, which assumes that the aerosol particle is a homogeneous dielectric sphere whose light scattering and absorbing properties are dependent on its complex refractive index (CRI) and its size relative to the incoming light's wavelength. For spherical particles, the spectral scattering and absorption efficiencies ( $Q_{\text{scat}}$  and  $Q_{\text{abs}}$ ) can be integrated over the aerosol particle size distribution to compute the scattering and absorption coefficients ( $C_{\text{scat}}$  and  $C_{\text{abs}}$ , respectively):

$$C_{\text{scat,abs}}(\lambda) = \int_{\log D_{\text{min}}}^{\log D_{\text{max}}} \left[ \frac{\pi D^2}{4} \times Q_{\text{scat,abs}}(\lambda, \text{CRI, D}) \times n^{\text{o}}(D) \right] d\log D,$$
(3)

where D is particle diameter,  $\lambda$  is the wavelength of the measurement source,  $d \log D$  is the logarithmic difference between the upper and lower diameter cutoffs of each bin, and  $n^o$  is the logarithmic size-resolved aerosol particle number concentration. The integral bounds  $\log D_{\min}$  and  $\log D_{\max}$  correspond to the  $d \log D$  of the smallest and largest bins of the particle size distribution. The term  $n^o$  is used per convention to represent the following:

$$n^{o} = \frac{\mathrm{dN}}{\mathrm{d\log D}}.$$
 (4)

Using these equations, we can "invert" the extrinsic measurements of absorption and scattering coefficients to determine the mean and spread of intrinsic properties of aerosol. This process is detailed in Section 2.4 along with mathematical definitions of the intrinsic and extrinsic ambient properties that are evaluated in this study.

In general, remote sensors are not as sensitive to particle number concentration as they are to particle surface area and volume concentrations. For particles larger than the remote sensor's observing wavelength, the remote sensor is most sensitive to particle cross-sectional area (i.e., surface area concentration). For particles smaller than the observing wavelength, the remote sensor is most sensitive to volume concentration. Given the sensitivity of remote sensors to surface area and volume concentration, this work also discusses the logarithmic size-resolved aerosol particle surface area concentration ( $a^{\circ}$ ) and logarithmic size-resolved aerosol particle surface area concentration for spherical particles in a given size range is defined as follows:

$$a^{\circ} = n^{\circ} \times \pi D^2 = \frac{\mathrm{dA}}{\mathrm{d\log D}}.$$
 (5)

Lognormal volume concentration of spherical particles in a given size range is defined as:

$$200 \quad v^{\circ} = n^{\circ} \times \frac{\pi D^{3}}{6} = \frac{\mathrm{dV}}{\mathrm{d} \log D}. \tag{6}$$

#### 2.2 ACTIVATE Mission Description

190

The ACTIVATE featured 162 coordinated science flights across six ACTIVATE deployments that occurred from 14 February 2020 to 18 June 2022. The six ACTIVATE deployments occurred between the following dates:

- 1. 14 February 12 March 2020,
- 2. 13 August 30 September 2020,
- 3. 27 January 2 April 2021,
- ♀ 13 May 30 June 2021,

- 5. 30 November 2021 29 March 2022,
- 6. 3 May 2022 18 June 2022.

210

- During the first five and a half ACTIVATE deployments, the majority of these flights were carried out using NASA Langley Research Center in Virginia as a base of operations, and the final half of the sixth ACTIVATE deployment was based in Bermuda. The extent of the North Atlantic region that was sampled during ACTIVATE was within bounds of 58–78°W and 28–42°N. The ACTIVATE methodology, sample region, and data set are described in more detail in Sorooshian et al. (2023). The ACTIVATE mission follows previous studies that aim to study aerosol-cloud interactions in the dynamic western North Atlantic environment (e.g., Quinn et al., 2019; Sorooshian et al., 2020; Dadashazar et al., 2021b, a; Corral et al., 2021; Painen Ret al., 2021).
- An important feature of the ACTIVATE data set is the extensive collocated advanced passive and active remote sensing and in-situ data. The ACTIVATE aircraft executed flights that can be broadly categorized into two mission types: "process studies" and "statistical surveys". This study focuses on statistical survey flights, where the lower-flying HU-25 Falcon aircraft collected in-situ data at various vertical levels (i.e., legs) in and above the marine boundary layer (MBL) for ~3.3 hours (Dadashazar et al., 2022b). During these statistical surveys, the Falcon would also make occasional vertical profiles (i.e., controlled ascents and descents) through the atmosphere. Simultaneously, the higher-flying King Air at approximately 9 km would conduct remote sensing and launch dropsondes while being spatially coordinated with the Falcon. These flights comprised 90% of missions and allowed for the efficient in-situ characterization of gas, cloud, aerosol, and meteorological quantities of the MBL across multiple flights and deployments (Dadashazar et al., 2022b; Sorooshian et al., 2023). As noted previously, the focus on spatial coordination of the two aircraft during the flights is beneficial for external consistency analysis, which is later described in Sect. 2.6.

#### 2.3 Measurements

#### **2.3.1** Remote Sensor Instrument Descriptions

The Second Generation High Spectral Resolution Lidar, HSRL-2, is an active lidar remote sensor that provides vertically resolved profiles of various aerosol and cloud properties for campaigns such as the Cloud, Aerosol and Monsoon Processes Philippines Experiment (CAMP2Ex; Reid et al., 2023), Deriving Information on Surface Conditions from COlumn and VER- rically Resolved Observations Relevant to Air Quality (DISCOVER-AQ; Sawamura et al., 2017), and ACTIVATE (Sorooshian et al., 2023). Unlike standard elastic backscatter lidars such as Cloud-Aerosol Lidar with Orthogonal Polarization (CALIOP), the HSRL-2 has the ability to measure total and molecular backscatter separately from which aerosol backscatter, extinction, and lidar ratio (LR) can be derived (Hair et al., 2008; Burton et al., 2016, 2018). The HSRL-2 has channels at 355 and 532 nm with an additional elastic backscatter channel at 1064 nm where the ambient extinction coefficient at 355 and 532 nm is retrieved from the measured lidar ratio. Because the HSRL-2 does not measure LR at 1064 nm, the 1064 nm extinction is derived

In this study, the HSRL-2 measurement of total ambient extinction coefficient at 532 nm serves as the standard relative to the in-situ-derived ambient extinction coefficient as was done in Sawamura et al. (2017). The HSRL-2 products include ambient vertically resolved idar ackscatter coefficient and linear depolarization ratio (LDR) at wavelengths of 355, 532, and 1064 nm and extinction coefficient at 355 and 532 nm wavelengths (Fernald et al., 1984; Hair et al., 2008; Burton et al., 2018). The HSRL-2 field of view is 1 mrad, which corresponds to a 9 m footprint for an aircraft at 9 km altitude.

- Complementing the HSRL-2 is the RSP, which is a passive polarimetric remote sensor that uses highly accurate multispectral and hyperangular photopolarimetric measurements to characterize aerosol and cloud properties (Cairns et al., 1999, 2003). The aerosol products are based on an optimal estimate using the Research Scanning Polarimeter Microphysical Aerosol Properties from Polarimetery (RSP-MAPP) algorithm (Stamnes et al., 2018). Fine- and coarse-mode aerosol optical and microphysical properties are retrieved using seven channels that measure the total and polarized radiance across the visible-shortwave spectrum (wavelength range = 410–2260 nm) with over 100 viewing angles between ±55°. The RSP has a field of view of 14 mrad, which results in a 126 m along-track footprint for an aircraft at 9 km altitude. As a result, the RSP provides accurate columnaveraged retrievals of aerosol optical and microphysical properties such as real refractive index (RRI), IRI, effective radius (reff), and single scattering albedo (SSA).
- The relevant King Air products are described in Table 1 along with their associated vertical resolutions, temporal resolutions, and uncertainties. Note that the native resolution of the extinction coefficients measured by the HSRL-2 is 225 m vertically and 60 seconds temporally. The provided HSRL-2 coefficients are smoothed from the subsampled resolution of 15 m × 1 s to the native resolution 225 m × 60 s by taking the arithmetic mean of all subsampled points within each native bin. In addition to analyzing the consistency of the standard HSRL-2 and RSP aerosol particle products, this study will analyze the consistency of the novel vertically resolved aerosol particle number concentration estimate (N; Schlosser et al., 2022). Complete details on the derivation of vertically resolved Neare discussed in Schlosser et al. (2022), but note that this quantity relies on the HSRL-3 Perived aerosol extinction coefficient at 532 nm and the RSP-derived aerosol extinction cross section at 532 nm.

#### 2.3.2 In-Situ Instrument Descriptions

In-situ measurements of size-resolved dry *N* are taken from the Scanning Mobility Particle Sizer (SMPS) (Model 3085 DMA, Model 3776 Condensation Particle Counter (CPC), and Model 3088 Neutralizer; TSI, Inc.) and a Laser Aerosol Spectrometer (LAS) (Model 3340; TSI, Inc.). The SMPS measures concentrations of particles with mobility D ranging in size from 2.97 to 94 nm at a 45-second temporal resolution (Moore et al., 2017). The LAS measures concentrations of particles with optical equivalent D ranging in sizes from 94 to 7500 nm at a 1-second temporal resolution (Froyd et al., 2019). The LAS sampled particles that were actively dried with a 6" Monotube dryer (Perma-Pure, Model 700) for all flights except the 30 from 14 May through 30 June, 2021 that were only dried passively. All SMPS data relied on passive drying from ram heating and a generally

**Table 1.** Summary of the King Air payload including relevant Second Generation High Spectral Resolution Lidar (HSRL-2) and Research Scanning Polarimeter (RSP) ambient aerosol particle products with associated native resolutions and uncertainties.

Instrument	Parameter Description	Vertical/Temporal	Uncertainty	
	8	Resolution		
	Total Extinction coefficient at 355, 532, and	225 m / 60 seconds	$0.01{\rm km^{-1}}$	
	1064 nm wavelengths <sup>*</sup>			
Second Generation	Total backscatter coefficient at 355, 532, and	30 m / 10 seconds	$0.2{\rm Mm^{-1}sr^{-1}}$	
High Spectral	1064 nm wavelengths			
Resolution Lidar	Total linear depolarization ratio (LDR) at 355 and	225 m / 10 seconds	2-5%***	
(HSRL-2)	532 1064 nm wavelengths			
	Column aerosol optical depth (AOD) at 355 and	-/60 seconds	0.02	
	532 nm wavelengths			
	Total, fine-mode, and coarse-mode hyper-	= / 4.167 seconds	0.04 / 0.015**	
	spectral column AOD from 410 to 2250 nm			
	wavelengths			
	Column-averaged total, fine-mode, and coarse-	-/4.167 seconds	21%	
Research	mode aerosol particle number concentration (N)			
Scanning	Column-averaged total, fine-mode, and coarse-	-/ 4.167 seconds	0.02 / 0.15 μm***	
Polarimeter (RSP)	moderfective adius (reff)			
•	Column-averaged total, fine-mode, and coarse-	- / 4.167 seconds	0.05 / 0.07***	
	mode effective variance $(v_{eff})$			
	Column-averaged total, fine-mode, and coarse-	= / 4.167 seconds	=	
	mode aerosol particle extinction cross-section			
	$(\sigma_{ m ext})$			
	Column-averaged total, fine-mode, and coarse-	- / 4.167 seconds	0.02 / 0.04***	
	mode single scattering albedo (SSA)			
	Column-averaged fine-mode real refractive in-	-/ 4.167 seconds	0.02	
	dex (RRI)			
	Column-averaged fine-mode imaginary refrac-	- / 4.167 seconds	0.002	
 	tive index (IRI)			

Petrieved HSRL-2 product.

warmer cabin temperature than ambient air. Note that all drying was done to an RH of  $\leq$ 40%. The  $N_{\odot}$  measurements provided

<sup>\*\*</sup> Uncertainty values are approximate and dependent on scattering levels.

<sup>\*\*\*</sup> Uncertainty values \*\*\* Uncertainty values \*\*\* Uncertainty values \*\*\* Uncertainty values \*\*\*

by the SMPS and LAS are provided at standard temperature and pressure (273.15 K and 1013 mb).

295

300

While the LAS has a measurement range up to 7.5 µm, the maximum cutoff D of the sample inlet prevents the measurement of particles with ambient D > 5 µm for ACTIVATE (McNaughton et al., 2007; Chen et al., 2011). The effective upper size cut is  $D = 5 \, \mu m$  for all 2020 data. For this data set, only particles with a maximum of dry optical D up to 3488 nm were used. This is done because the next logarithmically-spaced bin starts at 3488 nm and extends beyond the limit for efficient transmission into the isokinetic inlet. For 2021 and 2022 data sets, a cyclone was installed upstream of the nephelometers that results in a 1 µm aerodynamic cutoff for those data. The impact on the absorption coefficient from particles above 1 µm is assumed to be negligible in the calculation of extinction coefficients.

It is important to note that the optical particle size can be greater than the aerodynamic size by a factor of 1.2 to 1.8 depending on the particle density and shape. Additionally, the cyclone has a 50% efficiency at 1 µm. Due to the difference between the aerodynamic and optical particle sizes and the imperfect nature of the cyclone, we use a maximum cutoff diameter of 2 µm for the upper bound of the LAS size distribution. To further motivate this decision, using lower thresholds of 1.5 and 1.8 µm resulted in a success rate of 33% and 10%, respectively. There is also a decrease in the internal consistency as all measures of bias increase when a cutoff of less than 2 µm is used.

Another important detail to note is that the LAS particle sizing is calibrated using an assumed dry CRI and shape. The systematic error introduced by using an assumed dry CRI and shape is expected to be minimized by performing the LAS calibration with respect to spherical ammonium sulfate particles with dry CRI of 1.53 + 0i, which is among the most common aerosol species (Ebert et al., 2004; Sawamura et al., 2017). Furthermore, external mixtures of many aerosol species have an apparent RRI that falls between 1.5 and 1.58 (Li et al., 2023). If an external mixture of aerosols is dominated by a RRI outside of this range, it is likely that the assumptions of a spectrally flat CRI and sphericity are not longer valid. The SMPS sizing is calibrated using National Institute of Standards and Technology (NIST)-traceable polystyrene latex spheres, while size-dependant concentrations were calibrated in the laboratory using monodispersed aerosol and a reference CPC. These calibrations resulted in good stitching between the SMPS and LAS distributions and good consistency between the integrated number concentrations measured by ancillary CPC measurements (see Figure 7 of Sorooshian et al., 2023).

The in-situ optical measurements are taken by the nephelometer (Model 3563; TSI, Inc.) and the tricolor Particle Soot Absorption Photometer (PSAP) (Radiance Research) (Sorooshian et al., 2023). The nephelometer measures cabin dried (RH≤60%) and humidified (RH=85%) particle scattering coefficients ( $C_{\rm scat,RH≤60}$  and  $C_{\rm scat,RH=85}$ ) at wavelengths equal to 450, 550, and 700 nm at a 1-second temporal resolution (Ziemba et al., 2013). In addition to the scattering coefficients, the nephelometers also measure RH. The PSAP measures dry absorption coefficient ( $C_{\rm abs,RH=40}$ ) at 470, 532, and 660 nm at a 1-second temporal resolution (Mason et al., 2018). The PSAP sample stream is dried by heating the optical block to 35°C. The scattering coefficients are corrected for truncation errors using Anderson and Ogren (1998) and the absorption coefficients are corrected for

a transmittance and flow errors using Virkkula (2010). The parallel dry and humidified nephelometer deployment allows for scattering coefficients to be adjusted to any RH up to saturation (RH = 99%) through the computation of  $\gamma$  (Sawamura et al., 2017). This  $\gamma$  product relates scattering coefficients at some specified RH (RH<sub>specified</sub>) to dry measured scattering coefficients through the following:

315

320

325

$$C_{\text{scat}, \text{RH}_{\text{specified}}} = C_{\text{scat}, \text{RH}_{\text{measured}}} \times \exp\left(-\gamma \times \ln\left[\frac{100\% - \text{RH}_{\text{specified}}}{100\% - \text{RH}_{\text{measured}}}\right]\right),\tag{7}$$

where RH<sub>measured</sub> is measured by the cabin dried nephelometer. Note that in cases where the measured cabin RH is >40%, the measured  $C_{\text{scat},\text{RH} \leq 60}$  is adjusted to be scattering at an RH of 40% (i.e.,  $C_{\text{scat},\text{RH} = 40}$ ) using Eq. 7. For the purposes of this study, we will only use scattering and absorption data when all three channels of the nephelometer and PSAP have signals are above 1 Mm<sup>-1</sup> and 0 Mm<sup>-1</sup>, respectively.

Measurements of ambient liquid water content (LWC) and cloud drop number concentration ( $N_{\rm d}$ ) are used to classify insitu data as cloud-free, ambiguous, or cloud. This classification becomes important because ISARA retrievals are performed for cloud-free cases. Ambient LWC and  $N_{\rm d}$  are both derived from ambient particle size distribution measured by a Cloud and Aerosol Spectrometer (Droplet Measurement Technologies CAS; Baumgardner et al., 2001; Lance, 2012), a Fast Cloud Droplet Probe (SPEC FCDP; Kirschler et al., 2022), and a Cloud Droplet Probe (Droplet Measurement Technologies CDP; Sinclair et al., 2019). The CAS, CDP, and FCDP measure particles in the ambient D size ranges of 0.5–50  $\mu$ m, 2–50  $\mu$ m, and 3–50  $\mu$ m, respectively. Measurements are considered cloud-free where LWC is less than 0.001 g m<sup>-3</sup>, respectively (Schlosser et al., 2022). Because the CAS, CDP, and FCDP provide redundant measurements of LWC, this work relies on the CDP primarily and only uses FCDP for flights where the CDP was not being used. The CAS is only used as a backup for LWC in the case the CDP and the FCDP are unavailable.

In addition to applying a maximum LWC threshold, a sampling inlet flag is used to confirm that the Falcon aircraft was operating with the isokinetic inlet rather than the Counterflow Virtual Impactor (BMI Inc. CVI; Shingler et al., 2012), which is intended for collecting cloud residuals. The ambient aerosol particle size distribution measured by the CAS, the CDP, and the FCDP also help account for coarse aerosol particles when calculating the final properties of the ambient aerosol particles (see Section 2.4). To round off the suite of in-situ instruments is the Diode Laser Hygrometer (DLH), which provides ambient RH data. Ambient RH is used for the final calculation of ambient aerosol properties as described in Sect. 2.4. Note that the DLH measures water vapor density, which is used with ambient pressure and temperature data to derive ambient RH to an relative accuracy of 15% of the measured RH (Diskin et al., 2002). The relevant Falcon measurements are described in Table 2 along with their associated size ranges, temporal resolutions, and uncertainties.

**Table 2.** Summary of the relevant Falcon measurements and payload with associated size ranges, resolutions, and one standard deviation uncertainties.

Measurement	Instrument	Systematic uncertainty (accuracy)	Random uncertainty (precision	Size range	Native time resolution (s
Dry logarithmic size- resolved aerosol particle number concentration $(n^{\circ})$	Scanning Mobility Particle Sizer (SMPS)	10%	_	2.97 – 94.0 nm	45
Dry n°	Laser Aerosol Spectrometer (TSI LAS-3340).	10%	-	93.9 – 3487.5 nm	1
Dry scattering coefficient at 450, 550, and 700 nm wave-	Nephelometer at RH $\leq$ 40% (TSI–3563)	10%	2 Mm <sup>-1</sup>	<1 μm*	1
lengths.  Humidified scattering coefficient at 450, 550, and	Nephelometer at RH $\simeq$ 80% (TSI–3563)	10%	2 Mm <sup>-1</sup>	<1 μm*	1
700 nm wavelengths  Dry absorption coefficient at 470, 532, and 660 nm	Tricolor Particle Soot Absorption Photometer (PSAP)	7.5%	$1\mathrm{Mm}^{-1}$	<5 μm	1
wavelengths  Relative humidity (RH)  Liquid water content	Diode Laser Hygrometer (DLH) Cloud Droplet Probe (Droplet	7.5% <mark>10%</mark>	-	- 2 – 50 μm	0.05
(LWC), cloud drop number concentration $(N_{\rm d})$ , and	Measurement Technologies CDP)	10%	-	2 – 30 µm	ı
coarse-mode ambient $n^{\circ}$ LWC, $N_{d}$ , and coarse-mode ambient $n^{\circ}$	Cloud and Aerosol Spectrometer (Droplet Measurement Technolo-	10%	=	0.5 <mark>– 50 μm</mark>	1
LWC, $N_d$ , and coarse-mode ambient $n^\circ$	gies CAS) Fast Cloud Droplet Probe (SPEC FCDP)	10%	-	3 – 50 μm	1

<sup>\*</sup> For ACTIVATE 2020, this was <5 \(\mu\). See Sect. 2. For details.

#### 2.4 In-Situ Aerosol Retrieval Algorithm (ISARA) Description

The first step of this algorithm is to match all in-situ data to the lowest time resolution of the suite of instruments. In the case of ACTIVATE, the SMPS has the lowest time resolution of 45 seconds. The 45-second resolution is a shortcoming of the SMPS on an aircraft that can travel of 8 km across the ground in 45 seconds. As such, the external consistency analysis is most useful

from vertical profiles where the in-situ platform samples the column of air above an arbitrary ground point. Vertical profiles where the extent is more than 1 km are most useful for comparing with the column-averaged aerosol particle properties derived from the RSP-measurements. The data merge is handled by the NASA Airborne Science Data for Atmospheric Composition online merge tool (see www-air.larc.nasa.gov). Data in their native resolution are averaged to 45 seconds using the NASA merging tool. After this step, the SMPS and LAS size distributions are stitched at a diameter of 94 nm, which is the upper bound of the size-range by the SMPS and the lower bound of the LAS size-range.

350

After the size distribution measurements are stitched, ISARA is used to determine the aerosol optical and microphysical properties relevant to this study. Computation of scattering and absorption coefficients is accomplished using MOPSMAP (Bohren and Huffman, 2008; Gasteiger and Wiegner, 2018). As discussed above, the size range for the size-resolved number concentration measurements used in these retrievals is 3–3487.5 nm for ACTIVATE 2020 data, which is truncated to 3–2000 nm for ACTIVATE 2021-2022.

ISARA is a retrieval algorithm that uses dry and humidified (i.e., wet) aerosol measurements to retrieve the dry aerosol particle properties while accounting for changes in optical properties due to hygroscopicity, allowing the derivation of ambient aerosol properties. For these retrievals, we assume that the CRI does not change with wavelength (e.g., the CRI is spectrally flat), which is a good assumption for organic and sulfate aerosol species observed for much of ACTIVATE within the 450–700 nm range of wavelengths (Bain et al., 2019). Asso, as discussed previously, we have limited our calculations to classical Mie theory due to the assumption of particle sphericity. The first main step of the ISARA retrieval is calculating a total dry CRI since this is a critical parameter for Q and C as mentioned previously. This step focuses on retrieving CRI. Eq. 3 is rewritten as follows to denote the calculation of dry parameters (Eq. 8):

Figure 1 shows logarithmic size-resolved aerosol particle number concentration ( $n^{\circ}$ ), logarithmic size-resolved aerosol particle surface area concentration ( $a^{\circ}$ ), and logarithmic size-resolved aerosol particle volume concentration ( $v^{\circ}$ ) as a function of dry particle diameter ( $D_{dry}$ ) from all of the ACTIVATE 2020–2022 data. It is observed that the ACTIVATE data is mostly comprised of fine-mode particles with very low concentrations of coarse-mode particles.

A set of scattering and absorption coefficients are then calculated by iterating through dry RRI and IRI. The IRI is iterated from 0.00 to 0.08 in increments of 0.001, which is a range suited for typical aerosol particles in the ACTIVATE region. The RRI is iterated at 1.51, 1.52 1.53, 1.54, and 1.55 to capture small deviations in RRI from the 1.53 assumed by the LAS calibration curve. Given that the scattering is dominated by particles in the LAS size range, we expect to get a good agreement between the ISARA-derived scattering coefficient and that measured by the nephelometer. Note that this process uses the mid-point (i.e., the geometric mean) particle diameters from each SMPS and LAS channel. After the set of scattering and absorption coefficients

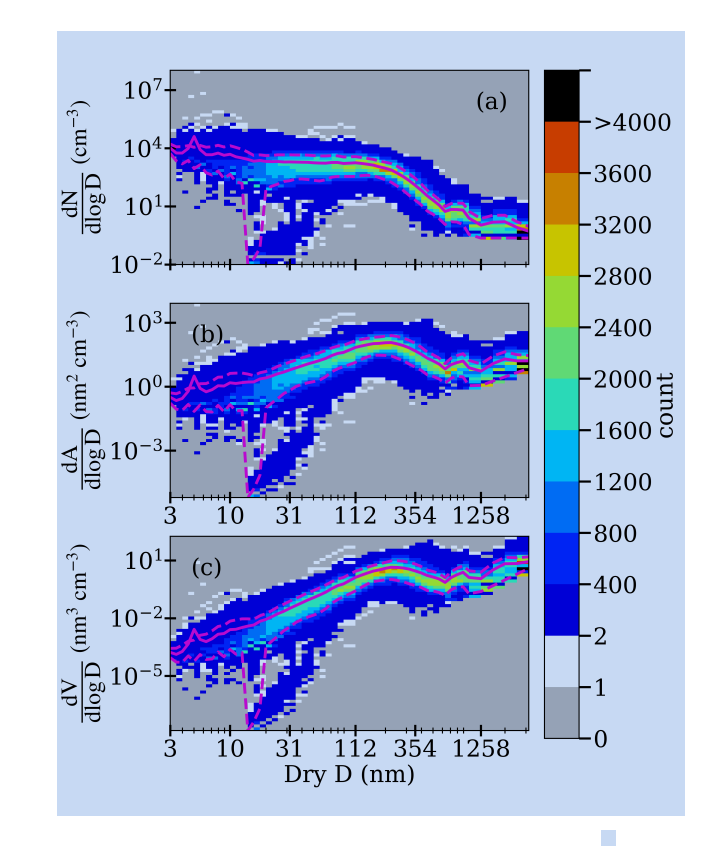


Figure 1. Heat map plot of logarithmic size-resolved aerosol particle (a) number concentration  $\left(n^{\circ} = \frac{dN}{d \log D}\right)$ , (b) surface area concentration  $\left(a^{\circ} = \frac{dA}{d \log D}\right)$ , and (c) volume concentration  $\left(v^{\circ} = \frac{dV}{d \log D}\right)$  versus dry particle diameter (D) measured from all ACTIVATE 2020–2022 data which is comprised of 34015 size distribution measurements at 45 second resolution. The solid line represents the arithmetic mean of each bin, the bottom and top dashed lines represent the 10th and 90th percentiles of each bin, respectively, and the color bar indicates density of points in a given area of the plot.

are calculated, ISARA retrieves a final value of total dry CRI ( $\overline{\text{CRI}}$ ) by taking the average of all valid CRI values. For a CRI to be valid for averaging, all three of the computed scattering coefficients must be within 20% of the corresponding measured dry scattering coefficient ( $\frac{|C_{\text{scat},\text{RH}=40}|}{|C_{\text{scat},\text{RH}=40}|}$  < 0.2) and all three of the calculated absorption coefficients must be within  $1\,\text{Mm}^{-1}$  of the measured absorption coefficients ( $|C_{\text{abs},\text{calc}}-C_{\text{abs},\text{RH}=40}|<1\,\text{Mm}^{-1}$ ). This method has been adapted from Sawamura et al. (2017) to include all three wavelengths. A summary of this retrieval step is provided in Fig. 2.

385

A final check is performed to ensure  $\overline{CRI}$  results in scattering and absorption coefficients that meet the same thresholds of 20% and  $1 \, \mathrm{Mm^{-1}}$ , respectively. Now that dry CRI has been determined, it is then necessary to retrieve the physical hygroscopicity parameter ( $\kappa$ ). Since the retrieval of  $\kappa$  relies on the same Mie theory principles as the previous step, Eq. 3 is rewritten to

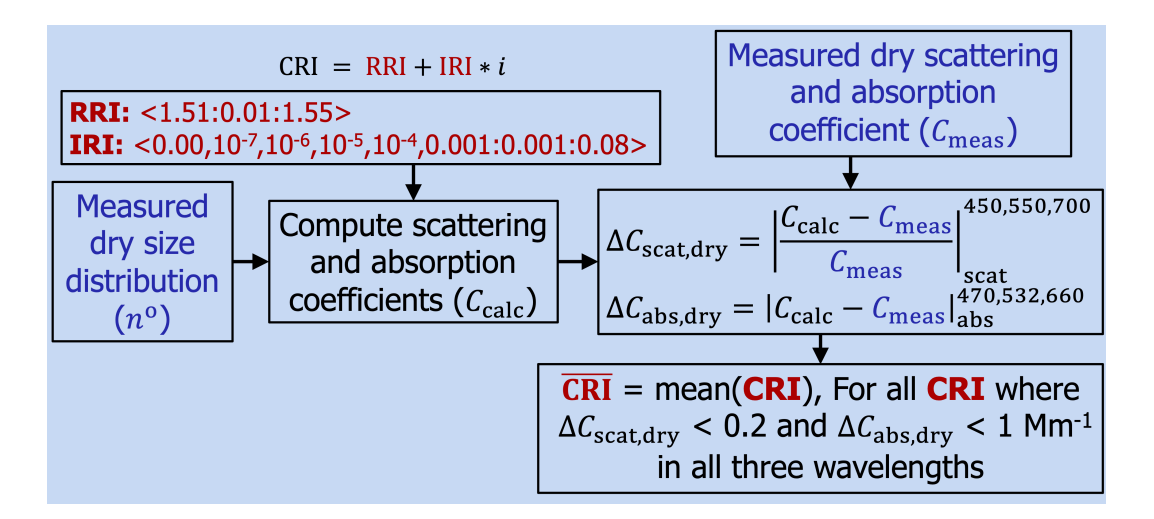


Figure 2. Flow chart of the dry CRI retrieval procedure. Blue text represents measured values, black text represents MOPSMAP-calculated values, and red text represents ISARA retrievals. The term  $C_{\rm calc}$  indicates calculated  $C_{\rm scat, dry}$  and  $C_{\rm abs, dry}$  while  $C_{\rm meas}$  indicates  $C_{\rm scat, RH=40}$  and  $C_{\rm abs, RH=40}$  from the nephelometer and PSAP instruments, respectively.

represent wet parameters (Eq. 9).

390 
$$C_{\text{scat,abs,wet}}(\lambda) = \int_{\text{log D}} \int_{\text{cost}} \left[ \frac{\pi \partial_{\text{opt}}^2}{\partial x} \times Q_{\text{scat,abs}}(\lambda, \text{CRI}_{\text{wet}}, D_{\text{wet}}) \times n^{\text{o}}(D_{\text{wet}}) \right] d\log D_{\text{wet}}.$$
 (9)

For the retrieval of  $\kappa$ , the forward-modeled humidified scattering coefficients are computed by adjusting for the impact that water uptake has on the increase in particle diameter as a result of hygroscopic growth to determine the humidified particle diameters and dry CRI. For spherical particles, both the scattering coefficients and particle diameters are related to  $\kappa$  by the  $g_f$ , which is defined as the ratio between the humidified and the dry particle diameters:

$$g_f = \frac{\text{Humidified Diameter}}{\text{Dry Diameter}} = \frac{D_{\text{wet}}}{D_{\text{QQ}}}.$$
 (10)

The  $g_f$  is related to  $\kappa$  by RH via the following parameterization from Petters and Kreidenweis (2007):

$$\frac{\nabla RH}{\exp\left(\frac{\alpha_w}{D_{\text{dry}}g_f}\right)} = \frac{g_f^3 - 1}{g_f^{\infty} - (1 - \kappa)} \tag{11}$$

where  $\alpha_w$  is the water activity. Water activity is a temperature-dependent function defined as follows:

$$\alpha_w = \frac{4\sigma_{s/w}M_w}{RTo},\tag{12}$$

where  $\sigma_{s/w}$ ,  $M_w$ , R, T, and  $\rho_w$  are surface tension of solute (i.e., aerosol) to water, molecular weight of water, ideal gas constant, temperature, and density of water, respectively. The values of  $\sigma_{s/w}$ ,  $\rho_w$ , and T are assumed to be  $0.072 \, \mathrm{J \, m^{-2}}$ ,

1000 kg m<sup>-3</sup>, and 298.15 K, respectively (Petters and Kreidenweis, 2007). For particles larger than 80 nm, this equation becomes (Zieger et al., 2013):

$$\left(\frac{D_{\text{wet}}}{D_{\text{drv}}}\right)^{3} = g = 1 + \kappa \times \frac{RH_{\text{wet}}}{100\% - RH_{\text{wet}}},$$
(13)

405 Where RH<sub>wet</sub> = 80%. Conceptually, hygroscopic growth results in the size distribution being shifted to the right by  $g_f$  and the distribution will widen if the size distribution is graphed with diameter on the x-axis. To account for the impact that water has on dry CRI, the humidified CRI is assumed to be the volume-weighted average between dry RRI and the CRI of water  $(CRI_{H_2O} = 1.33 + 0i)$ . The volume-weighted mixing model is used because it was found to be the most robust of a variety of possible mixing models by (Nessler et al., 2005). With this model, CRI can be written as a function of  $g_f$  (and consequently  $\kappa$  using Eq. 11) as follows:

$$\frac{\text{CRI}(g_f)}{\text{CRI}_{\text{dry}} + \text{CRI}_{\text{H}_2\text{O}} \times g_f^{\text{S}} - 1)}{g_f^3}.$$
(14)

With these relationships established, a set of wet scattering coefficients (i.e.,  $C_{\rm scat, wet}$ ) at 550 nm can now be calculated by iterating through  $\kappa$  from 0.00 to 1.40 in increments of 0.001, also a range typical of ACTIVATE's measured aerosol particles.

After calculating the set of forward-modeled  $C_{\rm scat, wet}$ , we use derive the "measured"  $C_{\rm scat, wet}$  (i.e.,  $C_{\rm scat, RH=80}$ ). The  $\gamma$  is derived from the tandem nephelometers as detailed in Sect. 2.3. The  $C_{\rm scat, RH=80}$  is obtained by applying Eq. 7 with the cabin dried measured scattering coefficient at 550 nm (i.e.,  $C_{\rm scat, RH=60}$ ) with the measured cabin RH, and by setting the specified RH to be 80%. The  $C_{\rm scat, RH=80}$  and  $C_{\rm scat, RH=40}$  are then used to calculate "measured" hygroscopic amplification factor (f(RH); Shingler et al., 2016) by rearranging Eq. 7 to be the following:

420 
$$f(RH) = \frac{C_{\text{scat},RH=80}}{C_{\text{scat},RH=40}} = \exp\left(-\gamma \times \ln\left[\frac{100\% - RH_{40}}{100\% - RH_{80}}\right]\right)$$
 (15)

After this step is performed, the smallest  $\kappa$  values are taken for computed  $C_{\rm scat, wet}$  that are within 1% of  $C_{\rm scat, RH=80}$  ( $\Delta C_{\rm scat, wet} < 1\%$ ). The smallest of these  $\kappa$  values is then taken to be the single effective  $\kappa$  ( $\overline{\kappa}$ ) for the fine-mode aerosol particles. A summary of this retrieval process is illustrated below (Fig. 3).

Oncol RI and red determine final humidified scattering coefficient and f(RH) are calculated for validation. Cumulative probability distributions of ISARA-derived IRI,  $\kappa$ , and f(RH) are shown or all ACTIVATE data (Fig. 4). It is observed that aerosol particles in the ACTIVATE region generally have low absorption (IRI  $\leq 0.01$ ) and low hygroscopicity ( $\kappa \leq 0.1$ ).

The ISARA-derived IRI and  $\kappa$  are combined with the measured ambient RH and dry size distribution data and are used to calculate ambient scattering and absorption coefficients ( $C_{\rm scat,amb}$  and  $C_{\rm abs,amb}$ , respectively) for the total (e.g., bulk) particle size-distribution ( $0.003 \le D \le 20 \,\mu\text{m}$ ), the fine-mode particle size-range ( $0.1 \le D \le 1 \,\mu\text{m}$ ), the coarse-mode particle size-range ( $1 \le D \le 20 \,\mu\text{m}$ ), and the optically active particle size-range ( $0.1 \le D \le 20 \,\mu\text{m}$ ). The ambient scatteriing and absorption

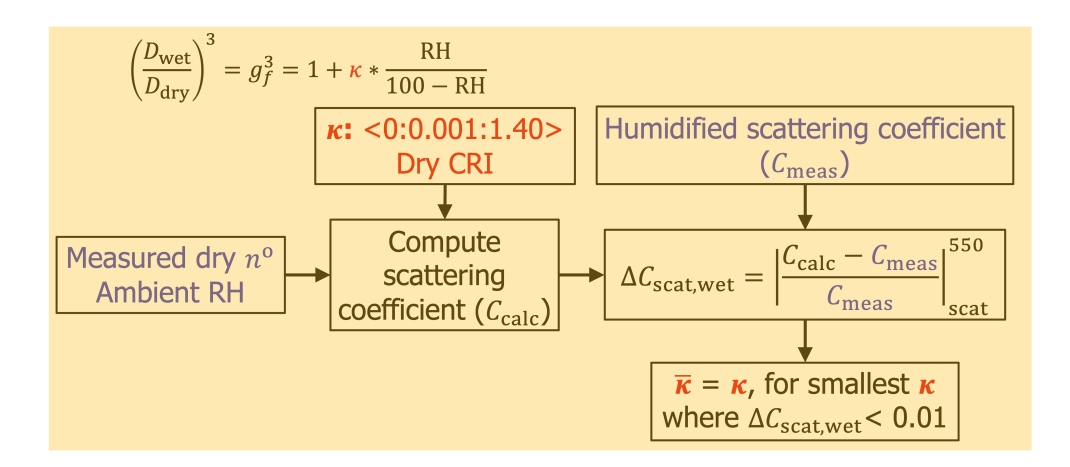
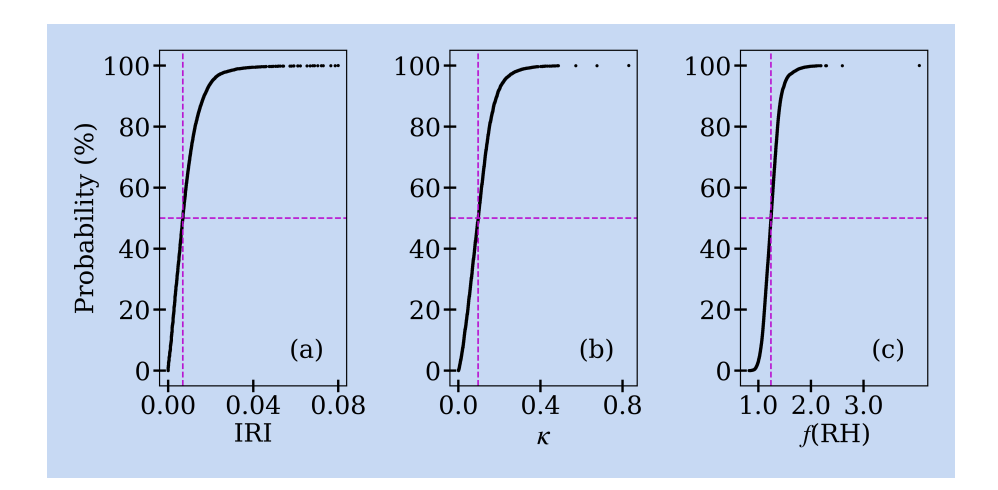


Figure 3. Flow chart of the physical hygroscopicity parameter ( $\kappa$ ) retrieval procedure. Blue text represents measured values, black text represents MOPSMAP-calculated values, and red text represents ISARA retrievals.  $C_{\rm calc}$  refers to the calculated scattering coefficient and  $C_{\rm wet}$  refers to the wet scattering coefficient derived from Eq. 7 and the dry scattering coefficient.



**Figure 4.** Cumulative probability distribution plots of retrieved (a) imaginary refractive index (IRI), (b) physical hygroscopicity parameter  $(\kappa)$ , and (c) hygroscopic amplification factor (f(RH)) derived from ACTIVATE 2020–2022 data. The intersection of the dashed magenta lines marks the medians of the data sets, which are 0.007, 0.095, and 1.24 for IRI, (b)  $\kappa$ , and (c) f(RH), respectively.

coefficients are calculate asing the following equation:

$$C_{\text{scat,abs,amb}}(\lambda) = \int_{\log D_{\text{min,amb}}} \left[ \frac{\pi D_{\text{a}}^2}{4} \times Q_{\text{scat,abs}}(\lambda, \text{CRI}_{\text{amb}}, D_{\text{amb}}) \times n^{\text{o}}(D_{\text{amb}}) \right] d\log D_{\text{amb}}.$$
(16)

Along with the ambient scattering and absorption coefficients, the other ambient aerosol microphysical and optical properties examined in this study are calculated across the particle ranges mentioned above. These properties are defined as follows (Note

that the following equations are at ambient conditions, but the "amb" subscript is omitted for brevity):

number concentration = 
$$N = \int_{\log D_{\min}}^{\log D_{\max}} n^{\circ} d \log D$$
 (17)

surface area concentration = 
$$A = \int_{\log D_{\text{max}}}^{\log D_{\text{max}}} a^{\circ} d \log D$$
 (18)

volume concentration = 
$$V = \int_{\log D_{\min}}^{\log D_{\max}} v^{\circ} d \log D$$
 (19)

effective radius = 
$$r_{\text{eff}} = \frac{V}{A}$$
 (20)

effective variance = 
$$v_{\text{eff}} = \frac{\int_{\log D_{\text{min}}}^{\log D_{\text{max}}} \left[ (0.5D - r_{\text{eff}})^2 \times a^o \right] d \log D}{r_{\text{eff}}^2 \times \int_{\log D_{\text{min}}}^{\log D_{\text{max}}} a^o d \log D}$$
 (21)

extinction coefficient = 
$$C_{\text{ext}}(\lambda) = C_{\text{scat}}(\lambda) + C_{\text{abs}}(\lambda)$$
 (22)

single scattering albedo = 
$$SSA(\lambda) = \frac{C_{scat}(\lambda)}{C_{ext}(\lambda)}$$
 (23)

backscatter coefficient = 
$$C_{\rm bsc}(\lambda) = C_{\rm scat}(\lambda) \times a_1(180^{\circ}),$$
 (24)

where  $a_1(180^\circ)$  is the phase function at  $180^\circ$  scattering.

$$\operatorname{lidar ratio} = \operatorname{LR}(\lambda) = \frac{C_{\operatorname{ext}}(\lambda)}{C_{\operatorname{bsc}}(\lambda)}$$
(25)

linear depolarization ratio = LDR(
$$\lambda$$
) = 
$$\frac{a_1(180^\circ) - a_2(180^\circ)}{a_1(180^\circ) + a_2(180^\circ)}$$
 (26)

Note that calculation of ambient N is restricted to the optically active particle size range (i.e., the portion of the distribution that significantly contributes to optical scattering and absorption (Schlosser et al., 2022)). Subsequent to the limitation of ambient N, we calculate aerosol particle extinction cross-section ( $\sigma_{\text{ext}}$ ) using the following relationship:

extinction cross section = 
$$\sigma_{\text{ext}}(\lambda) = \frac{\text{total } C_{\text{ext}}(\lambda)}{\text{optical } N}$$
, (27)

where to  $\mathbb{R}^{\mathbb{R}^{2}}$  where to  $\mathbb{R}^{2}$  is the extinction coefficient for the total size-distribution and optical N is the number concentration for the optically-active particle size range.

To perform the external consistency analysis outlined in Sect. 2.6, the coarse-mode contribution to the in-situ-derived total extinction, *N*, and SSA is derived from the CAS size distribution, with the assumption that coarse-mode particles have the microphysical and optical properties of hydrated sea salt. The assumptions made for this analysis are as follows: 1) the reference index of coarse-mode particles is set to that of water (CRI<sub>H2O</sub> = 1.33 + 0*i*), 2) the particles are fully hydrated, so no hygroscopic adjustment is applied, 3) they are spherical, and 4) the size distribution is truncated to diameters between 1,μm and 20,μm. If the CAS data are not available for a flight, CDP data are used for coarse-aerosol contribution. If both CAS and the CDP data are not available FCDP data are used.

#### 465 2.5 Synthetic Consistency Analysis Methodology

470

Synthetic data generation is accomplished using a Monte Carlo-style approach to synthetically create aerosol size distribution and composition data and apply theoretical measurement noise. This section details the synthetic data generation process, which involves: 1) creating ground-truth aerosol data, 2) generating synthetic in-situ measurements with appropriate measurement noise, and 3) using these synthetic measurements in ISARA to retrieve IRI and  $\kappa$ . The resulting optical and microphysical retrievals obtained from ISARA are detailed in Sect. 3.1.1.

The following discussion describes the process used to generate the synthetic data. Size distributions are generated by assuming the aerosol particles are spherical, since ISARA calculates resulting optical and microphysical properties using Mie theory as detailed in Sect 2.4. The synthetic ground truth size distributions are calculated for the particle diameter range of 2.97–3487.5 nm for each of the SMPS and LAS size bins to correspond with ACTIVATE size distribution data. To limit the number of unrealistic size distributions used for the retrievals, the shape of the size distribution is fixed and only the total number concentration is allowed to vary. Specifically, the shape of the size distribution is taken to be a 5-bin smoothed ACTIVATE-mean size resolved number concentration. The scale factor range of 0.5–10.0 is used for this analysis. This range is used to capture a large spread in particle concentrations within the ranges observed in the ACTIVATE data.

The physical hygroscopicity parameter ( $\kappa$ ) is then randomly chosen from the range of 0.00–1.40. The RH for this analysis is held at 80% and hence the corresponding  $g_f$  range is 1.00–1.77. The dry CRI is synthesized by assuming the RRI to be 1.53 while choosing IRI randomly from a range of 0.001–0.080. Finally, Eq. 3 is used to calculate  $C_{\rm scat, dry}$  at wavelengths of 450, 550, and 700 nm,  $C_{\rm abs, dry}$  wavelengths of 470, 532, and 660 nm, and  $C_{\rm scat, wet}$  at the 550 nm wavelength.

After generating the ground-truth aerosol data (i.e., synthetic size distribution, CRI, and  $\kappa$ ), synthetic in-situ measurements are created using the same randomly generated aerosol properties, the corresponding size distribution bins and ranges sampled by the instruments, and appropriate measurement noise. Measurement noise (using Table 2 as described below) is added to the synthetic data prior to performing the data processing and retrieval. The random (precision) and systematic (accuracy) measurement uncertainties from Table 2 are applied independently assuming they follow Gaussian probability distributions:

measurement = 
$$Y \times [1 + \text{rand}_n(\text{accuracy})] + \text{rand}_n\left(\frac{\text{precision}}{\sqrt{n_p}}\right),$$
 (28)

where n<sub>p</sub> is the SMPS resolution of 45 seconds and the *Y* is the synthesized value of the size resolved number concentration, dry spectral absorption and scattering coefficients, and humidified scattering coefficients. The rand<sub>n</sub> operator generates a random number from a Gaussian probability distribution, which is centered around the expected value of 0 and has a standard deviation that is given by the term in parenthesis. The accuracy from Table 2 noise is applied proportionally to every channel of each instrument to reflect the covariance of the channels. In other words, only one random sample is chosen per instrument. The precision uncertainty adjusted by dividing the uncertainties from Table 2 by the square root of the number of samples made in 45 seconds (i.e., n<sub>p</sub> = 45) to represent the increase in measurement precision due to averaging. This adjustment in precision due to averaging is not applied to the synthetic SMPS data as its native resolution is 45 seconds (i.e., n<sub>p</sub> = 1).

Equation 28 allows for measurement noise to be added to each synthetically-generated aerosol measurement. After adding the measurement noise to each simulated measurement, a total of 10000 synthetic aerosol distributions are inputted into MOPSMAP to generate IRI,  $\kappa$ , and consequently  $C_{\rm scat}$ ,  $C_{\rm abs}$ ,  $C_{\rm ext}$ , SSA, and f(RH) (results shown in Sect. 3.1.1). However, note that 26.49% synthetically-generated measurements did not fall within appropriate delta thresholds required for the successful retrieval of IRI and  $\kappa$  (see Figs. 2 and 3, respectively). The success rate of 73.51% can be improved by reducing measurement noise.

#### 510 2.6 External Consistency Analysis Process

485

The platform collocation process for this work is explained in complete detail in Schlosser et al. (2024), but is summarized in this section. Additionally, this section provides a summary of the methods used to column-average the in-situ data for comparison with the RSP data, which is described with more detail in Schlosser et al. (2022).

The first step of the process is to match the nearest HSRL-2 time stamp to each RSP scan. In order to search for cases with a substantial presence of fine-mode aerosol particles and low expected error, HSRL-2 and RSP aerosol optical depth (AOD) at 532 nm (Table 1) are used. Specifically, the HSRL-2 data are removed where the column AOD is <0.08. The RSP data are removed where fine-mode AOD is <0.1 and the normalized cost function of the RSP retrieval is >0.15. Because a significant presence coarse-mode particles would be atypical within the altitudes that are sampled by the Falcon, we attempt to limit the amount of coarse particles in the columns of compared data.

To limit the presence of coarse-mode aerosol particles in this analysis, the difference in HSRL-2-derived and RSP-derived total AOD must be <50% of HSRL-2-derived AOD or <0.05, whichever is greater. Additionally, coarse-mode AOD is limited to <0.1. Finally, to limit the scope of this analysis to spherical particles, LDR is used to filter out non-spherical from the data set (Burton et al., 2013). A LDR threshold of >13% was used to filter out non-spherical particles from the analysis. As discussed in Sect. 2.2 the ACTIVATE study region is characterized as a marine environment impacted by anthropogenic continental outflow, which is why the maximum LDR threshold of 13% was chosen.

To collocate the RSP and HSRL-2 data to the in-situ data, the collocation data files produced in Schlosser et al. (2024) are used to filter for times where the two aircraft are within 6 minutes and 15 km. For these comparisons, the ISARA-derived products are acquired where the Falcon aircraft was making a vertical profile through the atmosphere as identified in Sorooshian et al. (2023). Once the desired data are identified, the ISARA products data are weighted by extinction and averaged to the 225 m HSRL-2 bins or through the entire column for RSP comparisons. To provide aerosol source information for the discussion in Sect. 3.2, this study uses 96 hr back-trajectories from NOAA's Hybrid Single Particle Lagrangian Integrated Trajectory model (Stein et al., 2015). The input meteorological data were obtained from the North American Mesoscale Forecast System (NAM) with a horizontal resolution of 12 km (Rolph et al., 2017).

#### 2.7 Statistical Consistency Analysis Procedures

525

This section aims to define the statistical metrics used within this study. This also includes the specific metrics used to quantify how well ISARA-derived in-situ data close (i.e., agree) with internal, synthetic, and external consistency data sets. The mean  $(\bar{Z})$  of a set of data is given by:

$$\bar{Z} = \frac{\sum_{j=1}^{n_{\rm p}} Z(j)}{n_{\rm p}},\tag{29}$$

where Z(j) is an independent data point in the set Z and  $n_p$  is the total number of data points, respectively. The standard deviation (s) of a set of data is given by:

545 
$$s = \sqrt{\frac{\sum_{j=1}^{n_p} (Z(j) - \bar{Z})^2}{n_p}}$$
 (30)

In some cases, we use the weighted mean for a set of data, which is defined as:

$$\bar{Z}_{\text{weight}} = \frac{\sum_{j=1}^{n_p} \text{weight}(j) \times Z(j)}{\sum_{j=1}^{n_p} \text{weight}(j)},$$
(31)

where weight(j) is the weight associated with a given data point. Following the definition of the weighted mean, we define the weighted standard deviation ( $s_{weight}$ ) of a set of data as:

$$s_{\text{weight}} = \sqrt{\frac{\sum_{j=1}^{n_p} \text{weight}(j) \times (Z(j) - \bar{Z}_{\text{weight}})^2}{n_p}}.$$
(32)

The mean and standard deviation, or weighted mean and weighted standard deviation where noted, are useful for quantifying the common trends and fluctuations for a given set of data. The correlation coefficient (r) is used to quantify the strength of correlation between two collocated data sets and is defined as follows:

$$r = \frac{\sum_{j=1}^{n_p} [(X(j) - \bar{X}) \times (Y(j) - \bar{Y})]}{\sum_{j=1}^{n_p} [X(j) - \bar{X}]^2 \times \sum_{j=1}^{n_p} [Y(j) - \bar{Y}]^2},$$
(33)

Showhere X and Y are the set of in-situ and remote sensing aerosol measurements, respectively. Additionally, the p-value, which is the probability that the two parameters are not correlated (i.e., probability that the null-hypothesis is true), is used to quantify the statistical significance of the correlation (i.e., r). To quantify the difference between two measures of the same parameter, both bias and relative hias (RB) are used and defined as follows:

$$bias(j) = Y(j) - X(j)$$
(34)

560 and

$$RB(j) = \frac{bias(j)}{Y(j) + X(j)} \times 2 \times 100\%.$$
(35)

To quantify the systematic error of a set of comparable measures the range-normalized root-mean square deviation (NRMSD), the mean and standard deviation of bias (i.e.,  $MB \pm SB$ ), and the mean and standard deviation of RB (i.e.,  $MRB \pm SRB$ ) are discussed within the results. The NRMSD is defined as follows:

565 and

$$NRMSD = \frac{100\%}{\max(X) - \min(X)} \times \sqrt{\frac{\sum_{j=1}^{n_p} [Y(j) - X(j)]^2}{\bigotimes \bigotimes \bigotimes \bigotimes \bigotimes \bigotimes \bigotimes \bigotimes}}.$$
(36)

In this paper, statistical consistency is determined to be successful for a given ambient aerosol property in RNRMSD  $\approx 25\%$ , r > 0.8, and p-value < 0.05. Additionally, RSP is considered consistent for a given ambient aerosol property if the extinction

weighted mean  $\pm$  standard deviation values are within the RSP uncertainty values for that property listed in Table 2. If the results are within 5% of these values, they are considered "partially successful". Otherwise, they are considered unsuccessful.

#### 3 Results and Discussion

570

#### 3.1 Statistical Analysis

#### 3.1.1 Synthetic consistency

Now, consistency of ISARA-derived in-situ IRI and  $\kappa$  with synthetically-generated ones is presented. Before delving into these comparisons, synthetically-generated size distribution data are shown to provide context on how synthetic IRI and  $\kappa$  differ from ISARA-derived ones (Fig. 5).

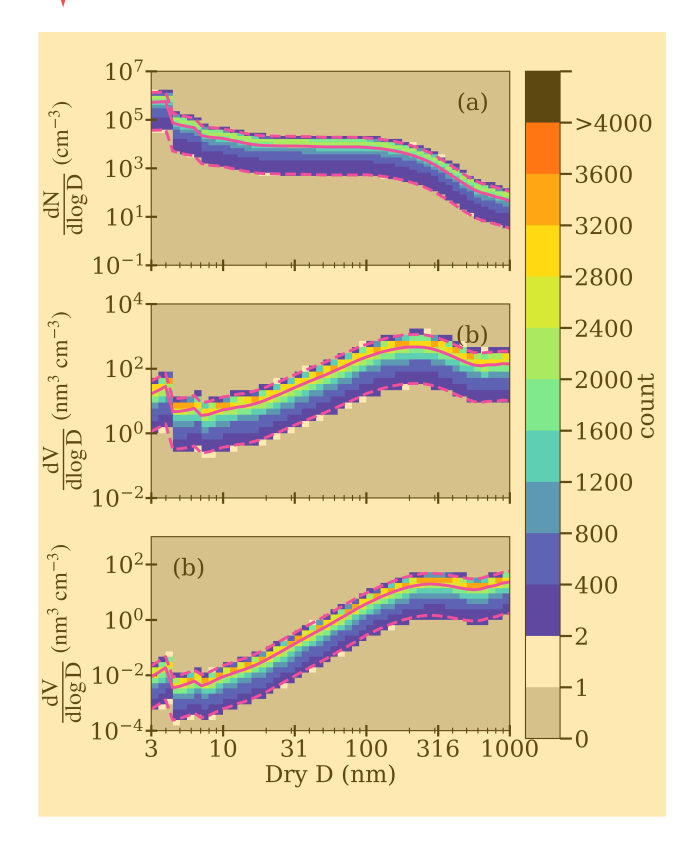


Figure 5. Logarithmic size-resolved aerosol particle (a) number concentration  $\left(n^{\circ} = \frac{dN}{d \log D}\right)$ , (b) surface area concentration  $\left(v^{\circ} = \frac{dA}{d \log D}\right)$ , and (c) volume concentration  $\left(v^{\circ} = \frac{dV}{d \log D}\right)$  versus dry particle diameter  $(D_{dry})$  from the 10,000 synthetic data points. The solid line represents the arithmetic mean of each bin, the bottom and top dashed lines represent the minimums and maximums of each bin, respectively, and the color bar indicates density of points in a given area of the plot.

The synthetic size distribution data are contained within the range of number and volume concentrations observed during AC-TIVATE (Fig. 1), but the synthetic data see overall much less variance. Future work could explore the impacts of adjusting the synthetic size distribution creation process to analyze the impact of low total concentration conditions.

580

585

As mentioned in Sect. 2.5, these theoretical size distributions are used to generate synthetic IRI and  $\kappa$  values. These synthetic values are now compared to corresponding ISARA-derived data (Fig. 6). Of the 10000 synthetically generated data points, 73.51% have successful retrieval of both IRI and  $\kappa$ . There are 5.28% lost between the IRI retrieval and the  $\kappa$  retrieval that corresponds to a success rate = 92.82%, which is close to the 95.03% success rate observed in the ACTIVATE retrieval of  $\kappa$ . It is observed that both IRI and  $\kappa$  comparisons show strong correlation coefficients of 0.99 and 0.98, respectively. Additionally, the biases (MRB  $\pm$  SRB) are centered near zero which are -0.9  $\pm$  20% and 3  $\pm$  28% for IRI and  $\kappa$ , respectfully. Based on these observations, the NRMSD for IRI and  $\kappa$  are 9% and 8%, respectively.

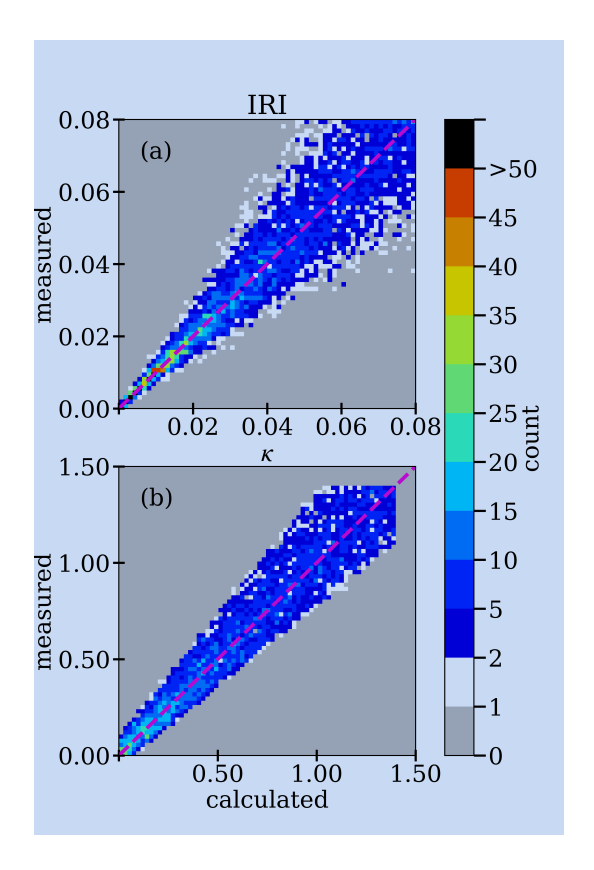


Figure 6. Heat map scatterplot of ISARA-retrieved versus synthetic (a) IRI (count = 7351, r = 0.99, MRB  $\pm$  SRB =  $-0.9 \pm 20\%$ , and NRMSD = 9%) and (b)  $\kappa$  (count = 6823, r = 0.98, MRB  $\pm$  SRB =  $3 \pm 28\%$ , and NRMSD = 8%). The dashed line represents the one-to-one line and the color bar indicates density of points in a given area of the plot.

In the algorithm's current state, it is expected that the ISARA-derived IRI and  $\kappa$  each agree within 30% under ideal assumptions of spherical particle shapes, a spectrally flat CRI, and a well-constrained RRI. Given the strong correlations and low biases, it is found that error as a result of forward modeling for spherical particles with constrained dry RRI (1.51  $\leq$  RRI  $\leq$  1.55) should not have a significant impact on the retrieval of a single effective IRI and  $\kappa$  from the size distribution, scattering coefficient, and absorption coefficient data measured during missions such as ACTIVATE.

To demonstrate the functionality of this analysis, the synthetic data generation and retrieval processes were repeated with zero measurement noise, which results in a rate of successful retrievals of 100%. Synthetic consistency analysis can be extended further to include non-spherical particles, particles without a constrained RRI, and increasing the number of successful retrievals under higher noise and lower signal conditions (e.g., lower aerosol particle concentrations, weakly scattering or weakly absorbing aerosol particles).

#### 3.1.2 Internal Consistency

595

600

610

615

As mentioned in the Introduction and Sect. 2, ISARA-calculated in-situ data are first closed with corresponding measurements from ACTIVATE's in-situ instruments to verify the robustness of the algorithm's retrieval method. First, ISARA retrievals of dry scattering and absorption coefficients are verified against corresponding measurements from the nephelometer and PSAP described in Sect. 2.3 (Fig. 7). A total of 19571 in-situ data points net the following criteria: (1) cloud-free conditions, (2) signal > 1 Mm<sup>-1</sup> in all three dry scattering measurements, (3) signal > 0 Mm<sup>-1</sup> in all three dry absorption measurements, and (4) at least three non-zero  $n^{\circ}$  measurements from both the SMPS and LAS instruments. Of these 19571 data points, there are 12319 points that had the successful retrieval of CM and 12319 had the successful retrieval of both CRI and  $\kappa$ . The observed successful retrieval rate  $\binom{\text{number of successful retrievals}}{\text{number of attempts}}$  for dry CRI alone is 62.95%, which is lower than the success rate of 73.51% observed for the synthetic consistency analysis (Sect. 3.1.1). Compared to the synthetic data set, the relatively lower retrieval success rate observed in the measured data set could be an indication that some of the measured data might be influenced by particles that violate the sphericity or the spectrally flat CRI assumptions. The lower retrieval success rate could be as a result of higher measurement noise than prescribed in the generation of the simulated data.

It is observed that for all three wavelengths, the two sets of dry scattering coefficient measurements correlate nearly perfectly (i.e., r = 0.99) and agree within 2% of each other in terms of NRMSD. Across all three channels, the ISARA-derived MRB is <10% compared the measured dry scattering coefficient, which indicates the measurements are systematically higher values than ISARA retrieves. Furthermore, the SRB ranges from 8 to 11% which suggests that there is an apparent non-zero bias in the ISARA forward model. Sources of this bias could be the assumption of a spectrally flat CRI and the assumption of a well constrained RRI of 1.53  $\pm$  0.02. Because this bias increases with increasing wavelength, it is possible that some of this discrepancy is due to larger particles that are more commonly comprised of dust, but this trend only accounts for a few percent difference in MRB accounts for a difference is a few percent of MRB. Finally, the MB  $\pm$  SB that resulted from the comparisons

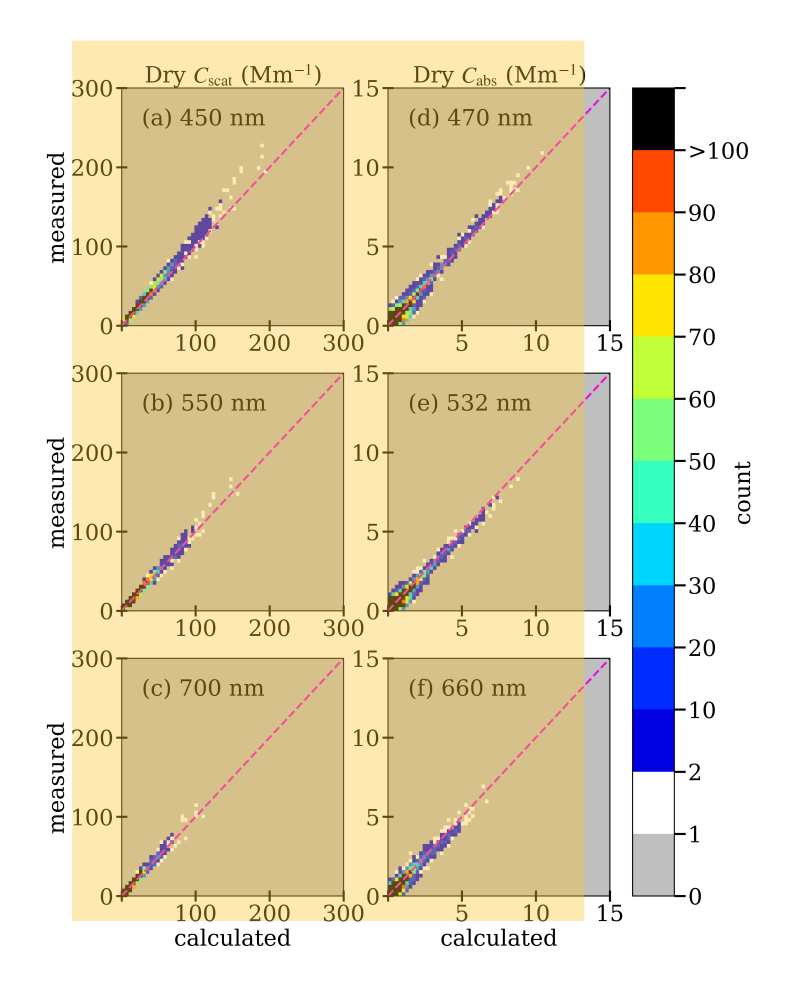


Figure 7. Heat map scatterplots of measured versus ISARA-derived in-situ values of dry scattering coefficient at (a) 450 nm (r = 0.99, MRB  $\pm$  SRB =  $9 \pm 8\%$ , NRMSD = 2%), (b) 550 nm (r = 0.99, MRB  $\pm$  SRB =  $3 \pm 8\%$ , NRMSD = 1%, and (c) 700 nm (r = 0.99, MRB  $\pm$  SRB =  $6 \pm 11\%$ , NRMSD = 1%). Also plotted are measured versus ISARA-derived in-situ values of dry absorption coefficient at (d) 470 nm (r = 0.96, MB  $\pm$  SB =  $0.03 \pm 0.30$  Mm<sup>-1</sup>, NRMSD = 3%), (e) 532 nm (r = 0.95, MB  $\pm$  SB =  $0.03 \pm 0.28$  Mm<sup>-1</sup>, NRMSD = 0.03

Section of the second of the

Dry absorption is also internally consistent as seen by strong r (0.96, 0.95, and 0.93) and NRMSD (3%, 3%, and 4%) values as with the scattering coefficient comparisons, the MB between the ISARA- and PSAP-derived dry absorption are small relative

to the measurement uncertainty. The  $\overline{MB} \pm \overline{SB}$  ranges from  $-0.03 \pm 0.28 \, \mathrm{Mm^{-1}}$  to  $0.03 \pm 0.30 \, \mathrm{Mm^{-1}}$ , which would indicate that the corresponding MRB values observed in the ISARA-derived absorption data are less reliable when the absorption signal is <1  $\mathrm{Mm^{-1}}$ . Other reasons for the MRB observed in the absorption comparisons could be the errors associated with size distribution measurements such as differences between optical and mobility particle diameters, loss of small and larger particles through the sampling system, and instrument counting efficiencies. Overall, internal consistency of the dry absorption coefficient is deemed successful, but it is important to keep these biases in the absorption and scattering coefficients in mind when calculating secondary optical properties that rely on it, such as  $C_{\rm ext}$  and SSA.

630

635

Now, ISARA retrievals of the wet scattering coefficient ( $C_{\text{scat,wet}}$ ) and f(RH) are evaluated to test how well the  $\kappa$  retrieval performs before calculating final ambient aerosol properties (Fig. 8).

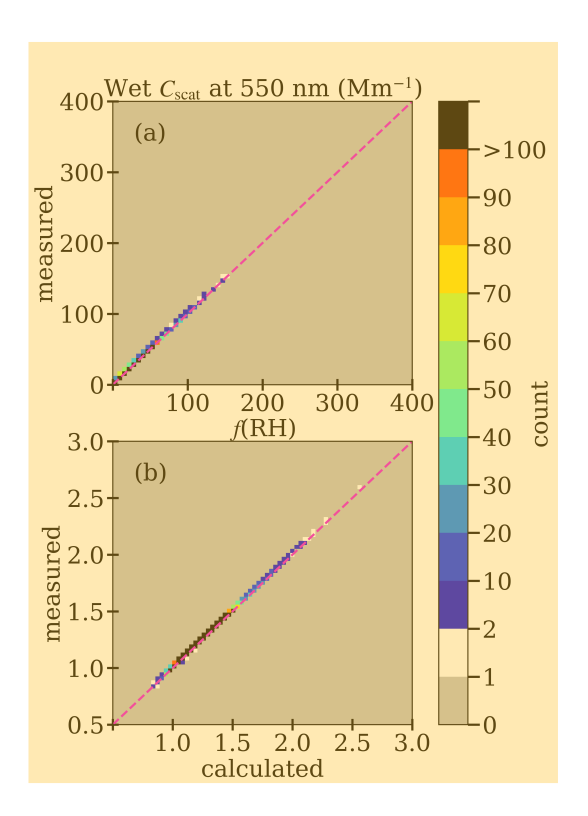


Figure 8. Heat map scatterplot of measured versus ISARA-derived in-situ values for (a) wet scattering coefficient ( $C_{\rm scat, wet}$ ) at 550 nm (r = 1.00, MRB  $\pm$  SRB =  $0.9 \pm 0.1\%$ , NRMSD = 0.2%) and (b) hygroscopic amplification factor (f(RH)) at 550 nm (r = 1.00, MRB  $\pm$  SRB =  $0.9 \pm 0.1\%$ , NRMSD = 0.4%) from the 10842 successful ISARA retrievals that resulted from the 2020–2022 ACTIVATE data. The dashed line represents the one-to-one line and the color bar indicates density of points in a given area of the plot.

Strong correlation coefficients (r = 1.00), strong agreement (NRMSD = 0.2% and 0.3%), and low bias (MRB  $\pm$  SRB = 0.9  $\pm$  0.1%) are seen between the two data with the two data with the strong of ISARA can involve implementing multiple  $\kappa$  parameters and

having a non-soluble mode, which has been shown to be useful in other consistency studies (van Diedenhoven et al., 2022). Based on the conditions detailed in Sect. 2.7,  $C_{\text{scat,wet}}$  and f(RH) at 550 nm are deemed internally consistent with the ISARA-derived values. The internal checks demonstrate that in a "perfect model" world the system works. In the next section we can examine how consistent the ISARA-derived aerosol products are as compared to the under-determined environmental system that relies on coordinated sampling by separate platforms and various retrieved ISARA and HSRL-2-products.

#### 3.1.3 External Consistency

After performing the procedures detailed in Sect. 2, ISARA-derived in-situ measurements of aerosol properties can be compared to coincident HSRL-2 and RSP retrievals for 2020–2022 ACTIVATE data. There are a total of 49 vertical profiles that have both an absence of clouds and meet the required collocation thresholds. Of the 49 vertical profiles, 10 of them have at least 3 points of comparison between the in-situ and HSRL-2 data. The ancillary information, RSP-, HSRL QQ at ISARA-derived QAOD, as well as the profile p-value resulting from the comparison of HSRL-2- and SARA-derived Cext at 532 nm for these 10 cases are listed in Tables 2000 QQ

**Table 3.** Ancillary data for each of the 10 case studies. Ancillary information includes the case number, the profile start and stop times, the associated RSP sample time, the minimum and maximum altitudes sampled by the Falcon (i.e., in-situ) aircraft, the number of smoke counts above 2.5 km identified by the HSRL-2, the RSP-derived total, fine-mode, and coarse-mode AOD, the HSRL-2-derived AOD, in-situ-derived AOD, and the horizontal separation between the Falcon and King Air. All dates and times are provided in coordinated universal time (UTC) and in the format "year-month-day" and "hour:minute:second", respectively.

					Altitu	de (km)			Platform
Case	Date	Profile	Profile	RSP	Min	Max	Sı	₽₩SRL��	paration
#		start	end	time			counts	LINO	(m)
1	2020-09-03	15:08:41	15:13:37	15:10:10	360	2460	0	0.84	<b>₽</b> ₩2
2	2021-03-04	17:59:53	18:05:45	18:03:16	458	1578	0	0.01	61
3	2021-03-09	16:29:26	16:32:52	16:32:20	387	1380	0	<b>?</b> 0.02	121
4	2021-03-12	17:45:09	17:50:21	17:45:38	413	1449	0	0.02	13685
5	2021-03-12	19:57:40	20:01:06	19:59:56	415	1535	0	0.02	7
6	2021-06-15	16:11:58	16:17:01	16:13:50	504	1268	4	0.02	1840
7	2022-03-03	14:56:17	15:22:48	15:19:24	238	4499	0	0.03	1829
8	2022-03-22	19:13:50	19:21:14	19:20:26	304	1683	0	0.04	82
<b>\tilde{V}</b>	<b>?</b> 2022-05-20	14:29:36	14:34:41	14:30:22	435	1466	18	0.03	<b>?</b> 319
10	2022-05-31	12:51:37	12:54:55	12:54:51	388	1256	0	0.02	<b>9</b> 893

The ancillary information (Table 3) includes the case number, the profile start and stop times, the associated RSP sample time, the minimum and maximum altitudes sampled by the Falcon aircraft, the number of smoke counts above 2.5 km identified by

Table Aerosol optical depth data derived from RSP, HSRL-2, and ISARA for each of the 10 case studies. Also should be resulting from the comparison of HSRL-2- and ISARA-derived  $C_{\text{ext}}$  at 532 nm, as well as the number of points available for comparison within each profle.

	I				C			
Şase Ş	Total	Fine	Coarse	HSRL-29	in-situ <mark></mark> AOD	<b>⇔</b> r	value a	<b>₹o\$</b>
7			<b>OOO</b>		ПОВ	'	<u>'</u>	
1	0.23	0.23	0.00	0.23	0.08	0.84	0.16	<b>₽</b> ₽
2	0.16	0.16	0.00	0.15	0.05	0.72	0.49	3
3	0.12	0.12	0.00	0.08	0.02	0.69	0.51	3
4	0.16	0.11	0.05	0.13	0.05	0.90	0.10	4
5	0.16	0.10	0.06	0.12	0.05	<b>≈</b> 0.97	0.16	3
6	0.19	0.18	0.01	0.18	0.01	0.58	0.60	3
7	0.12	0.10	0.02	0.08	0.08	0.95	0.00	13
8	0.20	0.11	0.09	0.15	0.08	0.80	0.10	5
9	0.45	0.39	0.06	0.45	0.09	<b>9</b> 0.28	0.72	<b>Ş</b> ↓
10	0.19	0.19	0.00	0.17	0.04	0.92	0.25	<b>888</b>

the HSRL-2, HSRL-2-derived column-averaged LDR, and the horizontal separation between the Falcon and King Air. All dates and times are provided in coordinated universal time (UTC) and in the format "year-month-day" and "hour:minute:second", respectively. The smoke counts above 2.5 km are taken to be the sum of all the altitude bins above 2.5 km that are flagged as smoke from from the HSRL-2 typing product (Burton et al., 2012).

660

Data from the 49 profiles provide the data for studying consistency of ambient  $C_{\text{ext}}$ ,  $C_{\text{bsc}}$ , LR and N. The ambient 355 nm  $C_{\text{ext}}$  and  $C_{\text{bsc}}$  are available for 82 points of comparison. The ambient 355 nm and 532 nm LR are available for 75 and 91 points of comparison. First, we present the results of the HSRL-2 and  $C_{\text{ext}}$ ,  $C_{\text{bsc}}$ , and LR consistency analysis (Figs. 9a-9h), which will be followed by a discussion of the N consistency analysis (Fig. 9i).

The HSRL-2- and ISARA-derived ambient  $C_{\rm ext}$  are moderately correlated with a r of 0.81, 0.69, and 0.44 for the 355, 532, and 1064 nm wavelengths, respectively. The p-value for the ambient  $C_{\rm ext}$  data are also much less that 1 (i.e., p-value <  $10^{-4}$ ) in all three wavelengths. The MRB  $\pm$  SRB are  $44 \pm 42\%$ ,  $35 \pm 52\%$ , and  $8 \pm 55\%$  for the 355, 532, and 1064 nm wavelengths, respectively. These MRB indicate that the in-situ data data is biased low from the HSRL-2, showing that the in-situ instruments retrieve lower values of  $C_{\rm ext}$  than the HSRL-2 throughout the ACTIVATE campaign. This finding is also supported by the NRMSD that ranges from 18 to 20%. This low bias result is also seen in Sawamura et al. (2017), which are MRB  $\pm$  SRB =  $31 \pm 5\%$  and  $53 \pm 11\%$ , for California and Texas, respectively. As discussed above, Sawamura et al. (2017)'s algorithm only considers fine-mode species in its analysis but ISARA accounts for the coarse-mode aerosol by using the CAS, CDP, or FCDP

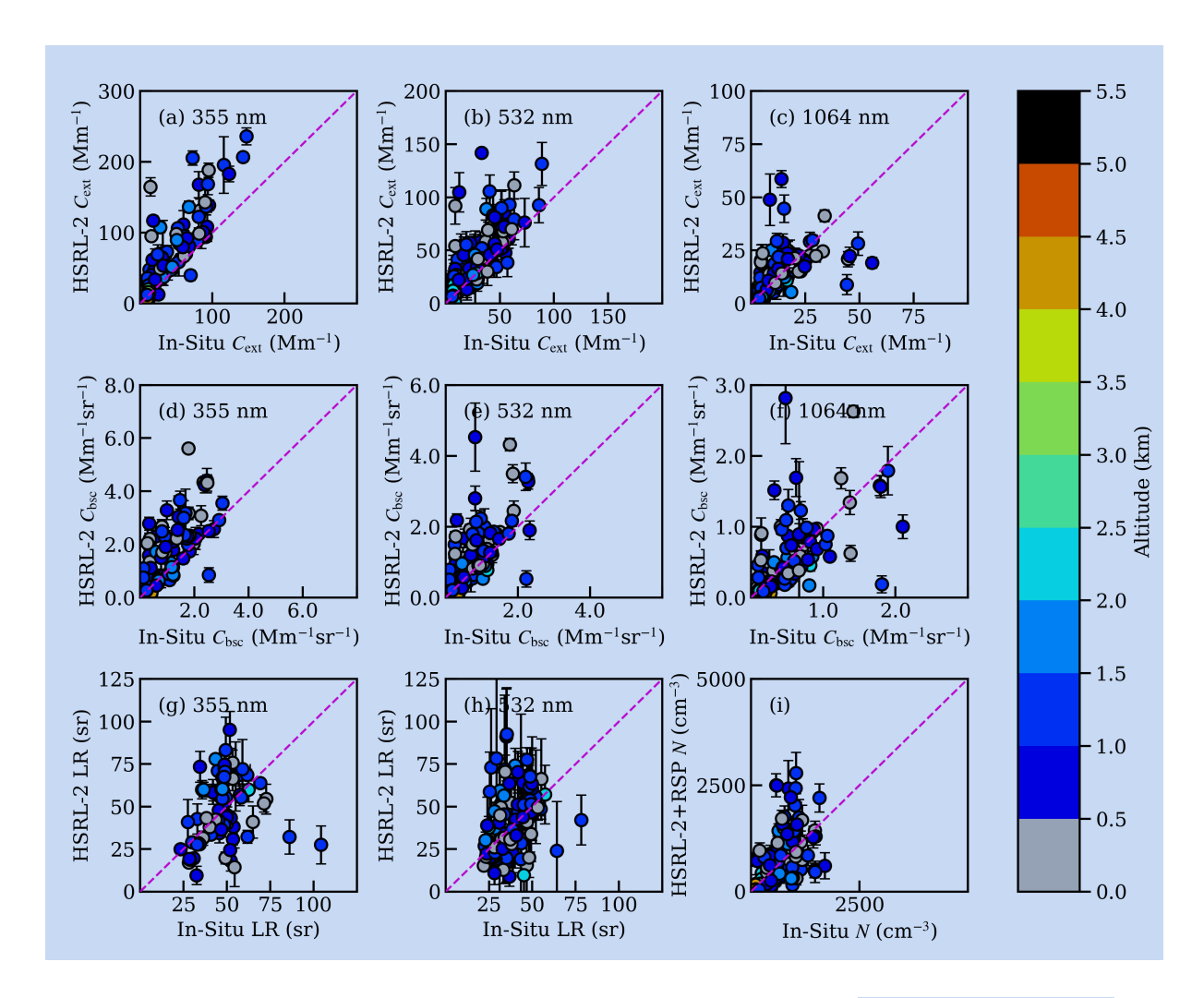


Figure 9. Scatterplots of the following vertically resolved aerosol particle properties: (a) 355 nm extinction coefficient ( $C_{\rm ext}$ ), (b) 532 nm  $C_{\rm ext}$ , (c) 1064 nm  $C_{\rm ext}$ , (d) 355 nm backscatter coefficient ( $C_{\rm bsc}$ ), (e) 532 nm  $C_{\rm bsc}$ , (f) 1064 nm  $C_{\rm bsc}$ , (g) 355 nm lidar ratio (LR), (h) 532 nm LR, (i) N, using 2020–2022 ACTIVATE data. The points of each panel are colored by the sample altitude in km, and the dashed line represents the one-to-one line. The error bars shown indicate the standard deviation of a given aerosol property. The consistency statistics for these data are shown in Table 5.

data and assuming the particles have the optical and microphysical properties of hydrated sea salt as described in Sect. 2.4. Similar to the internal consistency analysis, it is observed that the  $MB \pm SB$  are fairly small and range from  $1 \pm 11 \, \text{Mm}^{-1}$  to  $31 \pm 31 \, \text{Mm}^{-1}$ , which suggests that the MB are partially inflated by low signal or noisy conditions. This is further supported by observing the standard deviation (i.e., the error bars) of each point that often encompass the 1-to-1 line.

**Table 5.** Consistency statistics resulting from the comparisons of the vertically resolved aerosol properties of spectral  $C_{\rm ext}$ ,  $C_{\rm bsc}$ , and LR, as well as N. The consistency statistics shown correspond to the scatterplots shown on Fig. 9.

Aerosol Property	λ (nm)	$MB \pm SB$	MRB ±	NRMSD	r	<i>p</i> -	count
			SRB (%)	(%)		value	
	355	$30 \pm 31$	$44 \pm 42$	19	0.81	0.00	82
$C_{\mathrm{ext}}  (\mathrm{Mm}^{-1})$	532	$15 \pm 21$	$34 \pm 52$	18	0.69	0.00	98
	1064	$1 \pm 11$	$8 \pm 55$	20	0.44	0.00	98
	355	$0.7 \pm 0.9$	$42 \pm 59$	20	0.67	0.00	82
$C_{\rm bsc}~({\rm Mm^{-1}sr^{-1}})$	532	$0.4 \pm 0.7$	$29 \pm 55$	18	0.63	0.00	98
	1064	$0.03 \pm 0.46$	$-1 \pm 63$	17	0.54	0.00	98
I.D. (cr.)	355	$0.3 \pm 21$	$-5 \pm 42$	22	0.22	0.06	75
LR (sr)	532	4 ± 19	$1 \pm 47$	23	0.29	0.01	91
Optical $N$ (cm <sup>-3</sup> )	=	$135 \pm 581$	$0.5 \pm 68$	21	0.46	0.00	98

- The consistency statistics between HSRL-2- and ISARA-derived ambient  $C_{\rm bsc}$  and LR shows moderate to poor correlation especially for LR that has the lowest r and highest p-value, relative to  $C_{\rm ext}$ ,  $C_{\rm bsc}$ , and N. While the correlations are generally weaker for  $C_{\rm bsc}$  and LR, relative to  $C_{\rm ext}$ , the bias statistics indicate that the low correlation does not necessarily imply a lack of agreement.
- The  $C_{\rm bsc}$  MRB  $\pm$  SRB are  $42 \pm 59\%$ ,  $29 \pm 55\%$ , and  $-1 \pm 63\%$  for the 355, 532, and 1064 nm wavelengths, respectively. The MB  $\pm$  SB are  $0.7 \pm 0.9 \, \rm Mm^{-1} sr^{-1}$ ,  $0.4 \pm 0.7 \, \rm Mm^{-1} sr^{-1}$ , and  $0.03 \pm 0.46 \, \rm Mm^{-1} sr^{-1}$  for the 355, 532, and 1064 nm wavelengths, respectively. Finally, the NRMSD range from 17–20%, which decreases with increasing wavelength. From these statistics, we can observe that  $C_{\rm bsc}$  is constrained within  $1 \, \rm Mm^{-1} sr^{-1}$  in all three wavelengths, however the fidelity does decrease for the 1064 nm channel. As mentioned before, the 1064 nm channel is a retrieved product and as such this decrease in fidelity is somewhat expected.

The standard deviations in LR often encompass the 1-to-1 line and the MB is centered near zero for both wavelengths. The NRMSD resulting from the LR comparisons are 22 and 23% for the 355 and 532 nm wavelengths, respectively. The standard deviations in LR are much larger than what is observed in the  $C_{\rm ext}$  and  $C_{\rm bsc}$  comparisons. This combined with the range in observed LR in both wavelengths that is 20-100 sr suggests that this property is not well constrained.

It is observed that there is a systematic underestimation between ISARA- and HSRL-2-derived 355 and 532 nm  $C_{\rm ext}$  and  $C_{\rm bsc}$ , however this is more important at lower signals ( $C_{\rm ext}$ <50 Mm<sup>-1</sup> and  $C_{\rm bsc}$ <1 Mm<sup>-1</sup>sr<sup>-1</sup>). This discrepancy with the remote

sensors is likely due to the loss of particles from the diameter cutoff of the inlet and through the in-situ sampling pathways as discussed in the Introduction and undersampling of the coarse aerosol particles by the CAS, CDP, and FCDP. Although in-situ values are lower than the HSRL-2 ones, reasonable agreement is evident by the MB  $\pm$  SB ranges. These results indicate that further work is needed to fully close HSRL-2- and in-situ-derived  $C_{\rm ext}$  and  $C_{\rm bsc}$ , however the method does result in ambient extinction that meet the benchmarks set by previous works (e.g.,; Sawamura et al., 2017). By using ACTIVATE data for this analysis, the extinction product does work as expected even in conditions where coarse-mode sea salt is impacting the aerosol extinction. Future work can investigate improved methods for measuring coarse-mode aerosol from in-situ aircraft.

Next, jointly-retrieved HSRL-2+RSPQ and ISARA-derived N are compared (Fig. 9i and Table 5). These comparisons result in of 0.46, MRB  $\pm$  SRB of 0.5  $\pm$  68%, MB  $\pm$  SB of 135  $\pm$  581 cm 3  $\pm$  581 cm 4  $\pm$  710 to  $C_{\rm ext}$  and LR, the standard deviations in the HSRL-2+RSP-derived N often encompass the 1-to-1 line. While the correlation for vertically resolved  $N_{\rm LAS}$  (0.76 in Schlosser et al. (2022)), the r values from a profile that had a statistically significant correlations for 532 nm extinction (p-value < 0.05) is 0.95 for case 7 (see Table 3). Case 7 is also the only profile with more than 5 points for comparison and the conditions observed during this case study are such that it is investigated more in Sect. 3.2 Overall, the  $N_{\rm c}$  comparisons are considered to be closed relatively successfully when compared to results of Schlosser et al. (2022)'s evaluation of HSRL-2+RSP-derived  $N_{\rm c}$  using N derived from ISARA.

#### 3.2 Case Study

700

705

A case flight (Research Flight 131 on 3 March 2022) is chosen from Table 3 to examine how well ambient in-situ aerosol optical and microphysical measurements produced by ISARA compare with analogous RSP retrievals, which has not been shown in literature to date. Additionally, this case allows us to examine consistency of the vertically resolved properties for a case with an in-situ profile that extends more than 1 km. On this day, a "unicorn" module was performed (Sorooshian et al., 2023), where the Falcon aircraft performed a spiral from an altitude of 238 m to an altitude of 4,499 m to fully vertically-sample a rich aerosol layer identified as having urban/pollution and dust species as determined by the HSRL-2 aerosol typing algorithm (Burton et al., 2012). The Falcon spiral began at 14:56 UTC and ended at 15:22 UTC while the RSP sample time was at 15:19 UTC. The distance of the Falcon-in-situ spiral to the nearest valid RSP-King Air overpass was 1.8 km for this clear-sky aerosol scene over the ocean. No cloud contamination was identified in the HSRL-2, RSP, or camera images.

The four-day Hybrid Single Particle Lagrangian Integrated Trajectory (HYSPLIT) back trajectories are run at the altitudes of 500, 1500, and 3000 m above sea level, at 16:00 UTC on 3 March 2022, and at the location of the "unicorn" spiral (Fig. 10). These back trajectories use the meteorological data from the North American Mesoscale Forecast System (NAM)  $12 \times 12 \text{ km}^2$  HYSPLIT meteorological data set. From these back trajectories, it is evident that the air mass that was sampled during this case

was outflow from North America. This information indicates that the fine-mode particles being sampled were anthropogenic in origin and are likely sulfate-dominated mixtures with organic aerosol species. This is what would also be expected for this marine environment based on climatological evidence (Braun et al., 2021)...

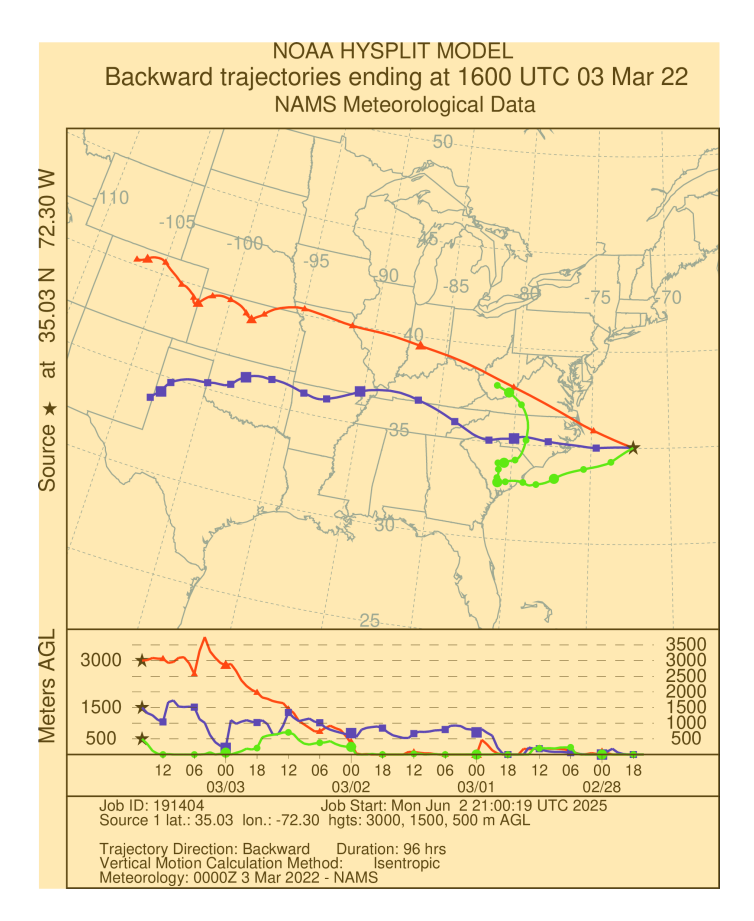


**Figure 10.** Four-day Hybrid Single Particle Lagrangian Integrated Trajectory (HYSPLIT) back trajectories end at the altitudes of 500, 1500, and 3000 m above sea level, at 16:00 UTC on 3 March 2022, and at the location of the "unicorn" spiral (Case 7) from Research Flight 131.

Figure 11 shows the profiles of vertically resolved  $C_{\rm ext}$ ,  $C_{\rm bsc}$ , and LR in all available wavelengths. Figure 12 shows the HSRL-2+RSP-derived N, HSRL-2-derived LDR, and the measured ameter RH. The remaining panels show the vertical profiles of ISARA-deriver, RRI, IRI, fine-mode SSA, total SSA, fine- and coarse-mode  $r_{\rm eff}$ , and fine- and coarse-mode  $v_{\rm eff}$ . These panels also illustrate how the column-averaged properties derived from the RSP compare to the vertically resolved data derived from the ISARA. The consistency statistics resulting from the comparisons of the vertically resolved aerosol properties are illustrated by Table 6.

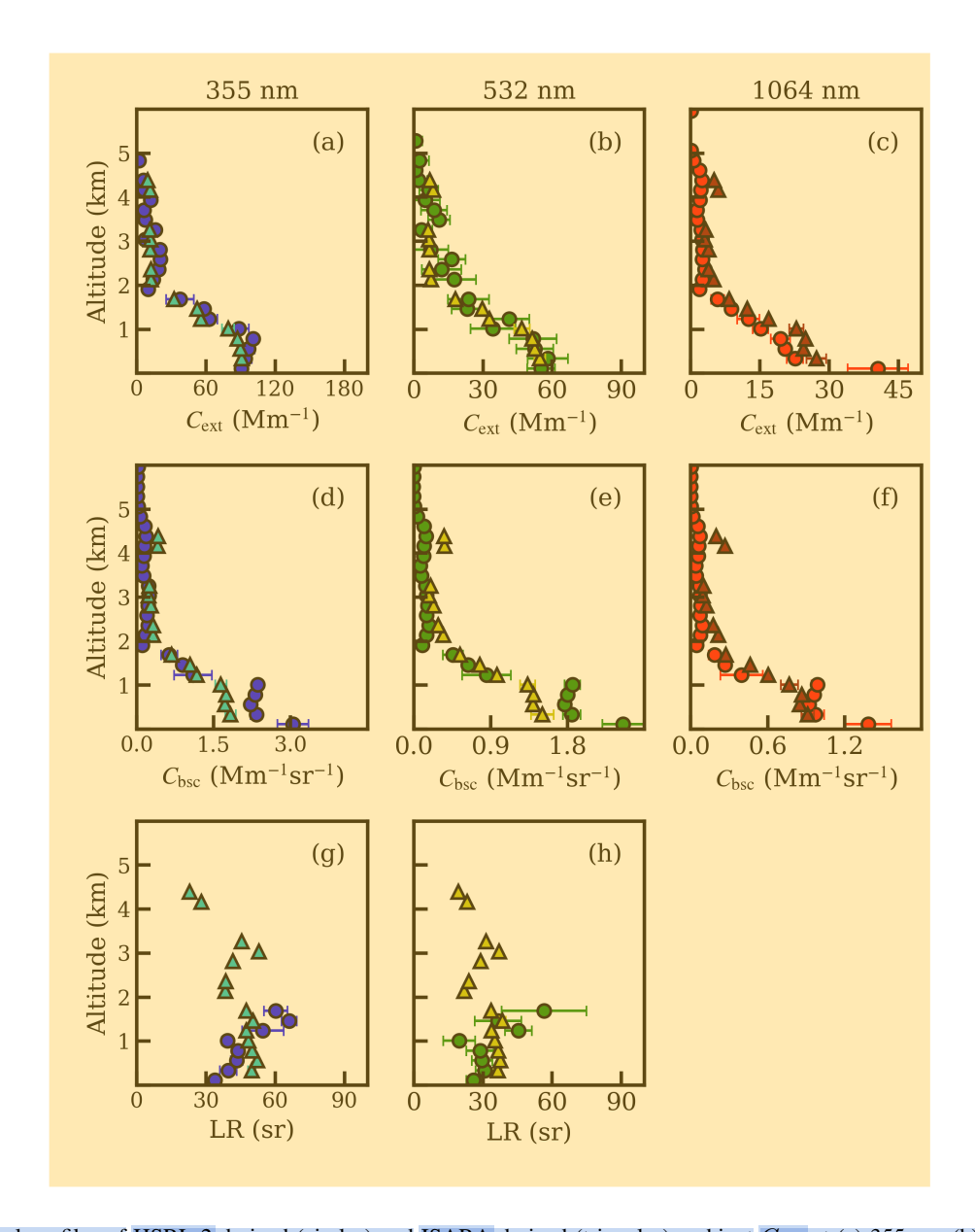


Figure 11. Vertical profiles of HSRL-2-derived (circles) and ISARA-derived (triangles) ambient  $C_{\rm ext}$  at (a) 355 nm, (b) 532 nm, and (c) 1064 nm wavelengths,  $C_{\rm bsc}$  at (d) 355 nm, (e) 532 nm, and (f) 1064 nm wavelengths, LR at (g) 355 nm and (h) 532 nm wavelengths, and (i) N from case study 7 that occurred during Research Flight 131 on 3 March 2022. The error bars shown indicate the standard deviation of a given aerosol property.

Although smoke aerosol could be present (Fig. 13), aerosol loading is low (AOD of 0.08 (HSRL-2) and 0.12 (RSP)) and the HSRL-2 is not detecting smoke counts in the vertical profiles shown (Table 3). Note that the vertical extent of the Falcon's profile is 4261 m. It appears there are increasing absorbing aerosol particles closer towards the surface, which is supported by

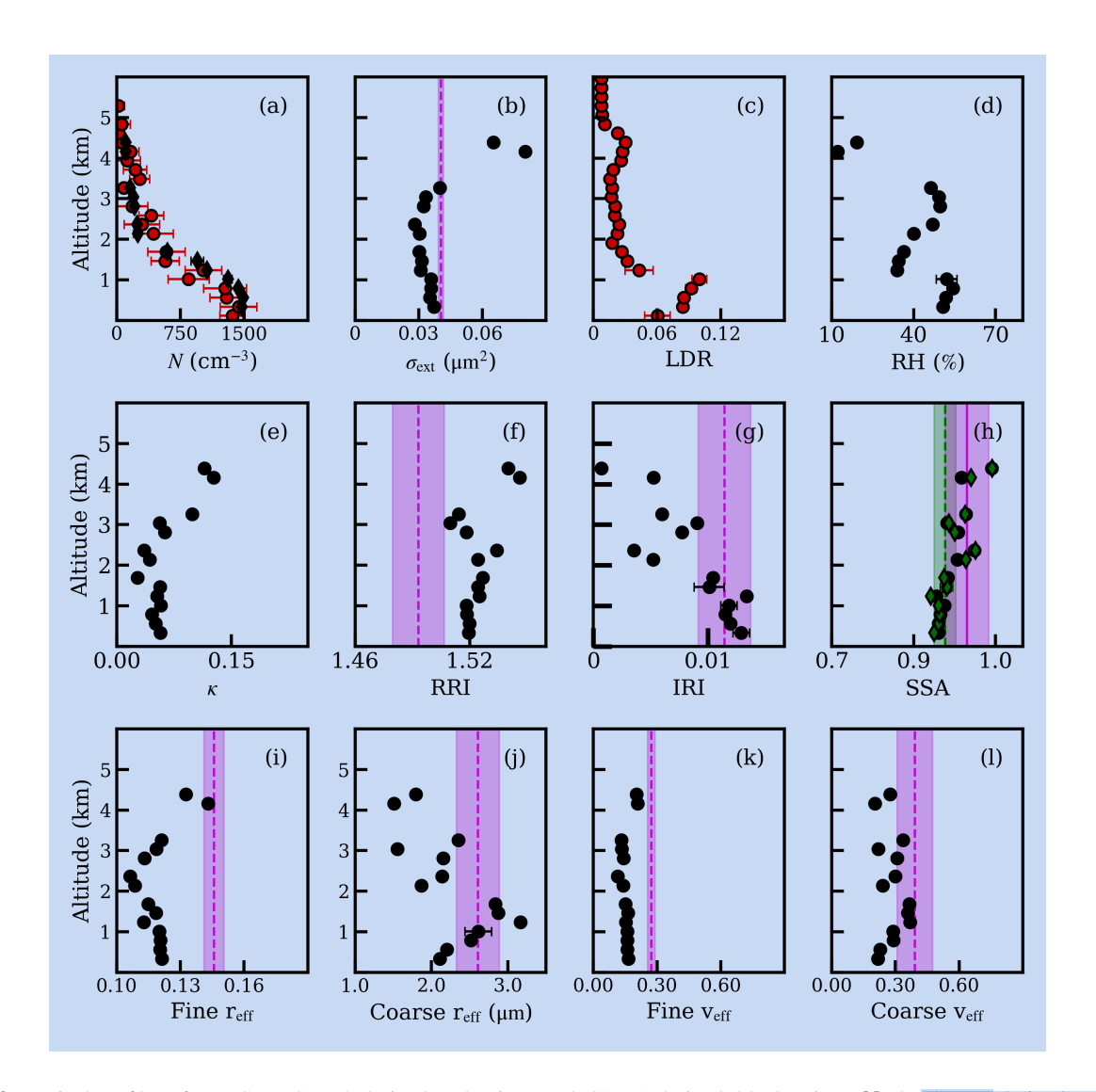


Figure 12. Vertical profiles of (a) RSP+HSRL-2-derived (red points) and ISARA-derived (black points) *N*, (b) ISARA-derived optical σ<sub>ext</sub> at 532 nm, (c) HSRL-2-derive pLDR, (d) in-situ-measured ambient RH, along with ISARA-derived (φκ, ambient (f) RRI, (g) IRI, (h) fine-mode (green diamonds) and total (black diamonds) SSA, (i) fine-mode effective radius (r<sub>eff</sub>), (j) coarse-mode r<sub>eff</sub>, (i) fine-mode effective variance (v<sub>eff</sub>), and (j) coarse-mode v<sub>eff</sub> from case study 7 that occurred during Research Flight 131 on 3 March 2022. The dashed magenta lines and shaded regions on panels (b) and (f)–(i) are the column-averaged properties and their associated uncertainties derived from the RSP. Panel (h) has an additional green dashed line and shaded region that represents the fine-mode SSA derived from the RSP. The error bars shown indicate the standard deviation of a given aerosol property. The ISARA-, HSRL-2- and RSP-derived total AOD are 0.08, 0.08 and 0.12, respectively.

ambient IRI values near 0.015 (Fig. 12g) and lower SSA values near 0.91 (Fig. 12h). There is also an increasing fine-mode  $r_{eff}$  and SSA seen above 2 km (Fig. 12h and 12i). It is also seen that ISARA-derived RH range is 40–55% that decrease 12 that decrease 12 and 12 are the second seco



**Figure 13.** NASA Worldview satellite image of fire presence (red points) during Research Flight 131 (3 March 2022) case flight with locations of LaRC and the Falcon flight spiral labeled. This image is used to identify sources of smoke on this day and comes from the VIIRS Fire and Thermal Anomalies product available from the NOAA-20 satellite (Schroeder et al., 2014).

at 4 km (Fig. 12d), which is not unexpected for a marine environment far off-shore in the winter (Sorooshian et al., 2019). It is also evident from the 1064 nm  $C_{\rm ext}$  and the 355, 532, and 1064 nm  $C_{\rm bsc}$ , that the near surface aerosol are distinctly different from the next highest data point (300 m). There is no available comparison with the ISARA-derived properties as the Falcon did not sample that low in the atmosphere. This finding is particularity important to consider when examining the column-average properties derived from the RSP. This near-surface elevated backscatter is likely due to sea salt near the ocean surface. This is also an important finding because it indicates that lowering the minimum sample altitude within the marine environment could help resolve some of the discrepancies seen in the statistical consistency analysis when comparing the vertically resolved comparisons. Additionally, it appears there may be the presence of an elevated aerosol layer with low concentrations at altitudes between 4 and 4.5 km.

the consistency statistics resulting from the vertically resolved data of case 7 further support that ISARA-derived aerosol properties are consistent with the HSRL-2-derived properties for the predominate aerosol particles observed in the North American outflow. Which exception of LR, he aerosol properties are well correlated with statistically significant correlations. Additionally, the MB are centered on, or near, zero for all the properties considered in this study. In contrast to the statistical analysis, this profile shows that ISARA-derived properties are slightly elevated in magnitude, relative to the HSRL-2-derived properties on average, however this appears to be true mostly for the aerosol particles above 1 km when observing  $C_{\text{ext}}$  and  $C_{\text{bsc}}$  the 355 and 532 nm wavelengths. The LR comparisons, where available, for this profile appear to be within the standard deviations

**Table 6.** Consistency statistics resulting from the comparisons of the vertically resolved aerosol properties of spectral  $C_{\text{ext}}$ ,  $C_{\text{bsc}}$ , and LR, as well  $\mathbb{Q}$ V. The consistency statistics shown correspond to the vertical profile from for case study 7 shown on Figures 11 and 12a.

									_
	Aerosol Property	$\lambda \Re m$	$^{\prime}$ MB $\pm$ SB	MRB 👺	NRMSD	$\mathbf{Q}_r$	<i>p</i> -	count	
				SRB (%)	(%)		value		
		355	$5\pm 5$	$9 \pm 30$	7	0.99	0.00	13	
	$C_{ m ext}~({ m Mm}^{-1})$	532	$0 \pm 6$	$-4 \pm 46$	11	0.95	<b>\$2.00</b>	13	
<b>63</b> 6		1064	$-3 \pm 2$	$-41 \pm 21$	15	0.99	0.00	13	
	∑ <sub>bsc</sub> (Mm <sup>-1</sup> sr	355	$0.1 \pm 0.3$	-17 ± 41	16	0.98	0.00	13	
		332 332	$0.0 \pm 0.3$	-25 ± 🗱	33 1633C	3(32X)	0.63	13	
		1064	$-0.1 \pm 0.1$	$-42 \pm 44$	15	0.97	0.00	13	
	LR (sr)	355	0 ± 10	-2 ± 20	39	-0.25	0.58	7	€3
		532	$-1 \pm 12$	$-7 \pm 33$	33	-0.54	0.21	7	<b>*</b>
	Optical N (cm <sup>-3</sup> )	_	-88 ± 169	$-12 \pm 36$	13	0.96	0.00	13	

With these conditions in mind, the vertical profile of ISARA results are then averaged using  $C_{\rm ext}$  for weights to provide column-averaged results (Table 7). The ISARA- and RSP-derived fine-mode  $v_{\rm eff}$  and  $r_{\rm eff}$  are in poor agreement, however the remaining aerosol properties are within the standard deviations of each other and appear to be in reasonable agreement for this profile. It is observed that 532 and 1064 nm total SSA derived from the RSP are elevated relative to the ISARA-derived counterparts. This is likely due to sea salt that was not sampled by the Falcon, which is supported by the elevated near surface  $C_{\rm bsc}$ .

Overall, in-situ and RSP derived products are in reasonable agreement under ideal conditions (Table 7). The only parameters that deviates significantly from the RSP retrieval error (see Stamnes et al., 2018) are ISARA-derived fine-mode reff and veff, which deviate by more than 0.03 µm and 0.11, respectively. This disagreement suggests that there are some fine-mode particles that are not being sampled by the Falcon. While 532 and 1064 nm total SSA are within the expected retrieval error, the RSP consistently sees higher total SSA in these channels. This disagreement in total SSA is likely due to coarse-mode sea salt aerosol particles being under-sampled by the in-situ instruments due to the low counting efficiency of the CDP of particles in this size range. This could also explain why the aerosol extinction coefficient retrieved by in-situ methods is systematically low as compared to HSRL-2 as resulted from the statistical analysis.

Table 7. Ambient optical and microphysical aerosol particle properties for case study 7 derived from the ISARA and the RSP. Ambient aerosol particle properties compared include the column-averaged properties of RRI, IRI, fine- and coarse-mode  $r_{eff}$  and  $v_{eff}$ , optical N and  $\sigma_{ext}$ , as well as spectral (355, 532, and 1064 nm) SSA for both the fine-mode and the total aerosol. The ISARA-derived extinction weighted average properties are shown with the weighted standard deviation and the RSP-derived properties are shown with the expected error from published sources where the measurement uncertainty was not available. The RSP retrieved fine- and coarse-mode AOD at 532 nm for this case is shown on Table 3.

Aerosol Property	ISARA	RSP	
Fine-mode $r_{\rm eff}$ ( $\mu$ m)	$0.12 \pm 0.005$	$0.15 \pm 0.005$	
Fine-mode v <sub>eff</sub>	$0.16 \pm 0.01$	$0.27 \pm 0.02$	
Coarse-mode r <sub>eff</sub> (µm)	$2.45 \pm 0.39$	$2.61 \pm 0.28$	
Coarse-mode veff	$0.28 \pm 0.06$	$0.39 \pm 0.08$	
Fine-mode RRI	$1.52 \pm 0.01$	$1.49 \pm 0.01$	
Fine-mode IRI	$0.017 \pm 0.004$	$0.017 \pm 0.003$	
Optical $\sigma_{\rm ext}$ at 532 nm ( $\mu {\rm m}^2$ )	$0.04 \pm 0.01$	$0.04 \pm 0.001$	
Optical $N$ (cm <sup>-3</sup> )	$1172 \pm 411$	$1250 \pm 246^{**}$	
Fine-mode SSA at 355 nm	$0.91 \pm 0.02$	$0.91 \pm 0.02^*$	
Total SSA at 355 nm	$0.91 \pm 0.02$	$0.94 \pm 0.04^*$	
Fine-mode SSA at 532 nm	$0.90 \pm 0.02$	$0.91 \pm 0.02^*$	
Total SSA at 532 nm	$0.91 \pm 0.02$	$0.95 \pm 0.04^*$	
Fine-mode SSA at 1064 nm	$0.82 \pm 0.04$	$0.84 \pm 0.02^*$	
Total SSA at 1064 nm	$0.91 \pm 0.02$	$0.97 \pm 0.04^*$	

<sup>\*</sup> Stamnes et al. (2018)

## 4 Conclusions

This study introduces the In-Situ Aerosol Retrieval Algorithm (ISARA), a retrieval framework developed to enable one-to-one comparison of aerosol properties across platforms in order to assess the consistency between field campaign remote sensing data sets and corresponding in-situ measurements, with the broader goal of driving rigorous external closure across field campaign aerosol measurement platforms. Because remote sensing instruments retrieve aerosol properties under ambient conditions, direct one-to-one comparison requires that dry in-situ measurements be converted to their ambient equivalents. ISARA performs this conversion by retrieving complex refractive index (CRI) and physical hygroscopicity parameter from a standard suite of in-situ measurements. This work extends the methods established by Sawamura et al. (2017) by attempting to account for coarse-mode aerosol particles in the bulk aerosol properties after retrieving the fine-mode CRI and κ. Similar the work of Tsekeri et al. (2017), we account for the contribution of coarse-mode (ambient particle diameter > 1.0 μm) particles using wing probe measurements. Incorporating the coarse-mode contribution enables more accurace.

<sup>\*\*</sup> Schlosser et al. (2022)

retrievals and supports rigorous consistency evaluation of field campaign aerosol data, as demonstrated in prior studies (Tsekeri et al., 2017). To evaluate the ability of ISARA to perform systematic consistency analysis, the algorithm is used on data from the Aerosol Cloud meTeorology Interactions oVer the western ATlantic Experiment (ACTIVATE) mission, which is chosen due to the campaign's large volume of statistically-rich aerosol measurements collected over three years of operations. Although the ACTIVATE region does feature a variety of aerosol and meteorological conditions, many of the ACTIVATE missions were carried out in cloud-free conditions without detectable influence from dust or smoke, making the data set well-suited for the consistency analysis performed in this study. Systematic consistency in this study is a three-fold effort: 1) internal consistency, which compares ISARA-retrieved ambient in-situ measurements with corresponding data from ACTIVATE's in-situ instruments, 2) synthetic consistency, where ambient in-situ data calculated from theoretical size distribution and composition data are compared to ISARA-derived in-situ values, and 3) external consistency, where ISARA-derived in-situ measurements are used to evaluate corresponding remote sensing retrievals from ACTIVATE's Second Generation High Spectral Resolution Lidar (HSRL-2) and Research Scanning Polarimeter (RSP) instruments.

Overall, this study demonstrates the successful retrieval of ambient aerosol properties from in-situ data in all three consistency analyses. Internal consistency analysis show near-perfect correlations ( $r \ge 0.96$ ), strong agreement (NRMSD = 1%), and generally low bias (absolute MRB < 10%) between ISARA-calculated and measured in-situ data for the dry scattering coefficient, dry absorption coefficient, wet scattering coefficient, and f(RH). Synthetic consistency analysis shows that errors in the forward model itself do not have a substantial influence on retrieved ambient aerosol properties since retrieved values of CRI and  $\kappa$  for spherical particles with expected measurement noise are found to have a forward modeling error (i.e., NRMSD) of 9% and 8%, respectively. Also, external consistency bet compared to have a forward modeling error (i.e., NRMSD) of 9% and some six deemed successful. The RSP-derived ambient total  $N_{\rm c}$  and fine-mode IRI, RRI, spectral SSA,  $r_{\rm eff}$ , and  $N_{\rm c}$  are all shown to be within expected error as compared to collocated in-situ data. These results demonstrate that external closure of RSP-derived aerosol properties is achievable, motivating future applications across a broader range of aerosol regimes and future field campaigns. However, it is important to note that the assumptions of perfectly spherical particles, of a single  $\kappa$  for all fine-mode particles, and of a spectrally flat CRI can still introduce limitations in the current version of ISARA's retrievals since aerosol particles from species such as sea salt, smoke, and dust can be non-spherical, can have inhomogeneous composition, and can have a wavelength-dependent CRI.

810

820

Only partial success is observed when comparing the HSRL-2-derived extinction coefficient ( $C_{\rm ext}$ ) to the corresponding IS-ARA-derived measurement, which are only moderately correlated (r ranging from 0.44 to 0.81) when considering all valid comparisons. Additionally, the in-situ-derived extinction coefficient and  $C_{\rm bsc}$  appears to be low (MRB range from 8044%) compared to the corresponding HSRL-2 measurement. This bias is likely due to under-sampling of coarse-mode aerosol species within the in-situ measurements. The total SSA is also underestimated by ISARA, as seen by ISARA-derived total SSA being low by 0.03 and 0.06 relative to the RSP-derived total SSA. Finally, the LR in both the 355 and 532 nm wavelengths appears to be poorly constrained and there is a general lack of consistency as evidence from the statistical analysis. For the unicorn

case, we do observe that LR is better constrained, but still shows a lack of correlation, a higher NRMSD, and wider spread in standard deviations, relative to  $C_{\rm bsc}$  and  $C_{\rm ext}$ .

While there are limitations and implicit errors in the ISARA retrievals, as discussed above, the results presented in this study demonstrate that these products are nonetheless valuable for evaluating the consistency of remote sensing measurements and supporting progress toward systematic external closure. The retrieved CRI and  $\kappa$  values are also relevant for aerosol and climate modeling applications, further extending the utility of this framework. In addition, the retrieval approach is both replicable and readily expandable. Although beyond the scope of this study, ISARA can be adapted for extended analyses that incorporate non-spherical particles, alternative coarse-mode representations, and non-soluble components of the aerosol distribution. Taken together, these capabilities suggest that the framework developed here can be applied beyond the ACTIVATE field campaign to advance efforts toward comprehensive closure of field campaign aerosol data sets.

Data availability. Source ACTIVATE airborne data are available with the ISARA-derived ambient aerosol properties through https://asdc.

larc.nasa.gov/project/ACTIVATE (ACTIVATE Science Team, 2020)

Author contributions. SD and JS prepared manuscript with all co-authors involved in review and editing. JS, SD, and SS performed all consistency analyses detailed in this study. All other authors provided input for the manuscript and/or participated in data collection and processing.

Competing interests. The authors declare that they have no conflict of interest.

835

840

Acknowledgements. Funding for this research was provided by the NASA ACTIVATE mission, a NASA Earth Venture Suborbital-3 (EVS-3) investigation funded by NASA's Earth Science Division and managed through the Earth System Science Pathfinder Program Office. A.S. and S.D. were supported by ONR grant N00014-22-1-2733. J.S.S. was supported by the NASA Postdoctoral Program at NASA Langley Research Center, administered by Oak Ridge Associated Universities under contract with NASA. J.S.R. was supported by the Office of Naval Research Code 322. The authors gratefully acknowledge the NOAA Air Resources Laboratory (ARL) for the provision of the HYSPLIT

transport and dispersion model and READY website (https://www.ready.noaa.gov) used in this publication. We wish to thank the pilots and aircraft maintenance personnel of NASA Langley Research Services Directorate for their work in conducting the ACTIVATE flights.

## References

870

- ACTIVATE Science Team: Aerosol Cloud meTeorology Interactions oVer the western ATlantic Experiment Data, https://doi.org/10.5067/SUBORBITAL/ACTIVATE/DATA001, 2020.
- Ajayi, T., Choi, Y., Crosbie, E. C., DiGangi, J. P., Diskin, G. S., Fenn, M. A., Ferrare, R. A., Hair, J. W., Hilario, M. R. A., Hostetler, C. A., Kirschler, S., Moore, R. H., Shingler, T. J., Shook, M. A., Soloff, C., Thornhill, K. L., Voigt, C., Winstead, E. L., Ziemba, L. D., and Sorooshian, A.: Vertical variability of aerosol properties and trace gases over a remote marine region: a case study over Bermuda, Atmospheric Chemistry and Physics, 24, 9197–9218, https://doi.org/10.5194/acp-24-9197-2024, 2024.
- Anderson, T. L. and Ogren, J. A.: Determining Aerosol Radiative Properties Using the TSI 3563 Integrating Nephelometer, Aerosol Science and Technology, 29, 57–69, https://doi.org/10.1080/02786829808965551, 1998.
  - Bain, A., Rafferty, A., and Preston, T. C.: The Wavelength-Dependent Complex Refractive Index of Hygroscopic Aerosol Particles and Other Aqueous Media: An Effective Oscillator Model, Geophysical Research Letters, 46, 10636–10645, https://doi.org/10.1029/2019GL084568, 2019.
  - Baron, P. and Willeke, K.: Aerosol Measurement: Principles, Techniques, and Applications, A Wiley-Interscience publication, Wiley, ISBN 9780471356363, https://books.google.com/books?id=nBpSAAAAMAAJ, 2001.
  - Baumgardner, D., Jonsson, H., Dawson, W., O'Connor, D., and Newton, R.: The cloud, aerosol and precipitation spectrometer: a new instrument for cloud investigations, Atmospheric Research, 59-60, 251–264, https://doi.org/10.1016/S0169-8095(01)00119-3, 13th International Conference on Clouds and Precipitation, 2001.
- Bohren, C. and Huffman, D.: Absorption and Scattering of Light by Small Particles, Wiley Science Series, Wiley, ISBN 9783527618163, https://books.google.com/books?id=ib3EMXXIRXUC, 2008.
  - Braun, R. A., McComiskey, A., Tselioudis, G., Tropf, D., and Sorooshian, A.: Cloud, Aerosol, and Radiative Properties Over the Western North Atlantic Ocean, Journal of Geophysical Research: Atmospheres, 126, e2020JD034113, https://doi.org/10.1029/2020JD034113, e2020JD034113, 2020JD034113, 2021.
- Burton, S. P., Ferrare, R. A., Hostetler, C. A., Hair, J. W., Rogers, R. R., Obland, M. D., Butler, C. F., Cook, A. L., Harper, D. B., and Froyd,
   K. D.: Aerosol classification using airborne High Spectral Resolution Lidar measurements methodology and examples, Atmospheric Measurement Techniques, 5, 73–98, https://doi.org/10.5194/amt-5-73-2012, 2012.
  - Burton, S. P., Ferrare, R. A., Vaughan, M. A., Omar, A. H., Rogers, R. R., Hostetler, C. A., and Hair, J. W.: Aerosol classification from airborne HSRL and comparisons with the CALIPSO vertical feature mask, Atmospheric Measurement Techniques, 6, 1397–1412, https://doi.org/10.5194/amt-6-1397-2013, 2013.
- Burton, S. P., Chemyakin, E., Liu, X., Knobelspiesse, K., Stamnes, S., Sawamura, P., Moore, R. H., Hostetler, C. A., and Ferrare, R. A.: Information content and sensitivity of the 3 [beta]+ 2 [alpha] lidar measurement system for aerosol microphysical retrievals, Atmospheric Measurement Techniques, 9, 5555, 2016.
  - Burton, S. P., Hostetler, C. A., Cook, A. L., Hair, J. W., Seaman, S. T., Scola, S., Harper, D. B., Smith, J. A., Fenn, M. A., Ferrare, R. A., Saide, P. E., Chemyakin, E. V., and Müller, D.: Calibration of a high spectral resolution lidar using a Michelson interferometer, with data examples from ORACLES, Appl. Opt., 57, 6061–6075, https://doi.org/10.1364/AO.57.006061, 2018.
  - Cairns, B., Russell, E. E., and Travis, L. D.: Research Scanning Polarimeter: calibration and ground-based measurements, in: Polarization: Measurement, Analysis, and Remote Sensing II, edited by Goldstein, D. H. and Chenault, D. B., vol. 3754, pp. 186 196, International Society for Optics and Photonics, SPIE, https://doi.org/10.1117/12.366329\_1999.

- Cairns, B., Russell, E. E., LaVeigne, J. D., and Tennant, P. M. W.: Research scanning polarimeter and airborne usage for remote sensing of aerosols, in: Polarization Science and Remote Sensing, edited by Shaw, J. A. and Tyo, J. S., vol. 5158, pp. 33 44, International Society for Optics and Photonics, SPIE, https://doi.org/10.1117/12.518320, 2003.
  - Chen, G., Ziemba, L. D., Chu, D. A., Thornhill, K. L., Schuster, G. L., Winstead, E. L., Diskin, G. S., Ferrare, R. A., Burton, S. P., Ismail, S., Kooi, S. A., Omar, A. H., Slusher, D. L., Kleb, M. M., Reid, J. S., Twohy, C. H., Zhang, H., and Anderson, B. E.: Observations of Saharan dust microphysical and optical properties from the Eastern Atlantic during NAMMA airborne field campaign, Atmospheric Chemistry and Physics, 11, 723–740, https://doi.org/10.5194/acp-11-723-2011, 2011.

- Corral, A. F., Braun, R. A., Cairns, B., Gorooh, V. A., Liu, H., Ma, L., Mardi, A. H., Painemal, D., Stamnes, S., van Diedenhoven, B., Wang, H., Yang, Y., Zhang, B., and Sorooshian, A.: An Overview of Atmospheric Features Over the Western North Atlantic Ocean and North American East Coast Part 1: Analysis of Aerosols, Gases, and Wet Deposition Chemistry, Journal of Geophysical Research: Atmospheres, 126, https://doi.org/10.1029/2020JD032592, e2020JD032592, 2020JD032592, 2021.
- Corral, A. F., Choi, Y., Collister, B. L., Crosbie, E., Dadashazar, H., DiGangi, J. P., Diskin, G. S., Fenn, M., Kirschler, S., Moore, R. H., Nowak, J. B., Shook, M. A., Stahl, C. T., Shingler, T., Thornhill, K. L., Voigt, C., Ziemba, L. D., and Sorooshian, A.: Dimethylamine in cloud water: a case study over the northwest Atlantic Ocean, Environ. Sci.: Atmos., 2, 1534–1550, https://doi.org/10.1039/D2EA00117A, 2022.
- Dadashazar, H., Alipanah, M., Hilario, M. R. A., Crosbie, E., Kirschler, S., Liu, H., Moore, R. H., Peters, A. J., Scarino, A. J., Shook, M.,
  Thornhill, K. L., Voigt, C., Wang, H., Winstead, E., Zhang, B., Ziemba, L., and Sorooshian, A.: Aerosol responses to precipitation along
  North American air trajectories arriving at Bermuda, Atmospheric Chemistry and Physics, 21, 16121–16141, https://doi.org/10.5194/acp21-16121-2021, 2021a.
- Dadashazar, H., Painemal, D., Alipanah, M., Brunke, M., Chellappan, S., Corral, A. F., Crosbie, E., Kirschler, S., Liu, H., Moore, R. H., Robinson, C., Scarino, A. J., Shook, M., Sinclair, K., Thornhill, K. L., Voigt, C., Wang, H., Winstead, E., Zeng, X., Ziemba, L., Zuidema, P., and Sorooshian, A.: Cloud drop number concentrations over the western North Atlantic Ocean: seasonal cycle, aerosol interrelationships, and other influential factors, Atmospheric Chemistry and Physics, 21, 10499–10526, https://doi.org/10.5194/acp-21-10499-2021, 2021b.
  - Dadashazar, H., Corral, A. F., Crosbie, E., Dmitrovic, S., Kirschler, S., McCauley, K., Moore, R., Robinson, C., Schlosser, J. S., Shook, M., Thornhill, K. L., Voigt, C., Winstead, E., Ziemba, L., and Sorooshian, A.: Organic enrichment in droplet residual particles relative to out of cloud over the northwestern Atlantic: analysis of airborne ACTIVATE data, Atmospheric Chemistry and Physics, 22, 13 897–13 913, https://doi.org/10.5194/acp-22-13897-2022, 2022a.
  - Dadashazar, H., Crosbie, E., Choi, Y., Corral, A. F., DiGangi, J. P., Diskin, G. S., Dmitrovic, S., Kirschler, S., McCauley, K., Moore, R. H., Nowak, J. B., Robinson, C. E., Schlosser, J., Shook, M., Thornhill, K. L., Voigt, C., Winstead, E. L., Ziemba, L. D., and Sorooshian, A.: Analysis of MONARC and ACTIVATE Airborne Aerosol Data for Aerosol-Cloud Interaction Investigations: Efficacy of Stairstepping Flight Legs for Airborne In Situ Sampling, Atmosphere, 13, https://doi.org/10.3390/atmos13081242, 2022b.
- Diskin, G. S., Podolske, J. R., Sachse, G. W., and Slate, T. A.: Open-path airborne tunable diode laser hygrometer, in: Diode Lasers and Applications in Atmospheric Sensing, edited by Fried, A., vol. 4817, pp. 196 204, International Society for Optics and Photonics, SPIE, https://doi.org/10.1117/12.453736, 2002.
- Ebert, M., Weinbruch, S., Hoffmann, P., and Ortner, H. M.: The chemical composition and complex refractive index of rural and urban influenced aerosols determined by individual particle analysis, Atmospheric Environment, 38, 6531–6545, https://doi.org/10.1016/j.atmosenv.2004.08.048, contains Special Issue section on Measuring the composition of Particulate Matter in the EU, 2004.

- Fernald, F. et al.: Analysis of atmospheric lidar observations- Some comments, Applied Optics, 23, 652–653, https://doi.org/10.1364/AO.23.000652, 1984.
- Ferrare, R., Hair, J., Hostetler, C., Shingler, T., Burton, S. P., Fenn, M., Clayton, M., Scarino, A. J., Harper, D., Seaman, S., Cook, A.,

  Crosbie, E., Winstead, E., Ziemba, L., Thornhill, L., Robinson, C., Moore, R., Vaughan, M., Sorooshian, A., Schlosser, J. S., Liu, H.,

  Zhang, B., Diskin, G., DiGangi, J., Nowak, J., Choi, Y., Zuidema, P., and Chellappan, S.: Airborne HSRL-2 measurements of elevated aerosol depolarization associated with non-spherical sea salt, Frontiers in Remote Sensing, 4, https://doi.org/10.3389/frsen.2023.1143944, 2023.
- Field, C., Barros, V., Dokken, D., Mach, K., Mastrandrea, M., Bilir, T., Chatterjee, M., Ebi, K., Estrada, Y., Genova, R., Girma, B., Kissel, E.,
  Levy, A., MacCracken, S., Mastrandrea, P., and White, L.: IPCC, 2014: Summary for policymakers. In: Climate Change 2014: Impacts,
  Adaptation, and Vulnerability, vol. 1, Cambridge University Press, 2014.
  - Froyd, K. D., Murphy, D. M., Brock, C. A., Campuzano-Jost, P., Dibb, J. E., Jimenez, J.-L., Kupc, A., Middlebrook, A. M., Schill, G. P., Thornhill, K. L., Williamson, C. J., Wilson, J. C., and Ziemba, L. D.: A new method to quantify mineral dust and other aerosol species from aircraft platforms using single-particle mass spectrometry, Atmospheric Measurement Techniques, 12, 6209–6239, https://doi.org/10.5194/amt-12-6209-2019, 2019.

- Fu, G., Hasekamp, O., Rietjens, J., Smit, M., Di Noia, A., Cairns, B., Wasilewski, A., Diner, D., Seidel, F., Xu, F., Knobelspiesse, K., Gao, M., da Silva, A., Burton, S., Hostetler, C., Hair, J., and Ferrare, R.: Aerosol retrievals from different polarimeters during the ACEPOL campaign using a common retrieval algorithm, Atmospheric Measurement Techniques, 13, 553–573, https://doi.org/10.5194/amt-13-553-2020, 2020.
- Gasteiger, J. and Wiegner, M.: MOPSMAP v1.0: a versatile tool for the modeling of aerosol optical properties, Geoscientific Model Development, 11, 2739–2762, https://doi.org/10.5194/gmd-11-2739-2018, 2018.
  - Hair, J., Hostetler, C., Cook, A., Harper, D., Ferrare, R., Mack, T., Welch, W., Izquierdo, L., and Hovis, F.: Airborne high spectral resolution lidar for profiling aerosol optical properties, Applied Optics, 47, 6734–6752, https://doi.org/10.1364/AO.47.006734, 2008.
  - Hussein, T., Maso, M. D., Petäjä, T., Koponen, I. K., Paatero, P., Aalto, P. P., Hämeri, K. J., and Kulmala, M.: Evaluation of an automatic algorithm for fitting the particle number size distributions, Boreal Environment Research, 10, 337–355, 2005.
  - Kirschler, S., Voigt, C., Anderson, B., Campos Braga, R., Chen, G., Corral, A. F., Crosbie, E., Dadashazar, H., Ferrare, R. A., Hahn, V., Hendricks, J., Kaufmann, S., Moore, R., Pöhlker, M. L., Robinson, C., Scarino, A. J., Schollmayer, D., Shook, M. A., Thornhill, K. L., Winstead, E., Ziemba, L. D., and Sorooshian, A.: Seasonal updraft speeds change cloud droplet number concentrations in low-level clouds over the western North Atlantic, Atmospheric Chemistry and Physics, 22, 8299–8319, https://doi.org/10.5194/acp-22-8299-2022, 2022.
- 960 Knobelspiesse, K., Cairns, B., Ottaviani, M., Ferrare, R., Hair, J., Hostetler, C., Obland, M., Rogers, R., Redemann, J., Shinozuka, Y., Clarke, A., Freitag, S., Howell, S., Kapustin, V., and McNaughton, C.: Combined retrievals of boreal forest fire aerosol properties with a polarimeter and lidar, Atmospheric Chemistry and Physics, 11, 7045–7067, https://doi.org/10.5194/acp-11-7045-2011\_2011.
  - Kulkarni, P., Baron, P., and Willeke, K.: Aerosol Measurement: Principles, Techniques, and Applications, Engineering professional collection, Wiley, ISBN 9780470387412, https://books.google.com/books?id=2VtsSKLsMY8C, 2011.
- Lance, S.: Coincidence Errors in a Cloud Droplet Probe (CDP) and a Cloud and Aerosol Spectrometer (CAS), and the Improved Performance of a Modified CDP, Journal of Atmospheric and Oceanic Technology, 29, 1532 – 1541, https://doi.org/10.1175/JTECH-D-11-00208.1, 2012.
  - Li, X., Gupta, D., Eom, H.-J., Kim, H., and Ro, C.-U.: Deliquescence and efflorescence behavior of individual NaCl and KCl mixture aerosol particles, Atmospheric Environment, 82, 36–43, https://doi.org/10.1016/j.atmosenv.2013.10.011, 2014.

- Di, Y., Bai, B., Dykema, J., Shin, N., Lambe, A. T., Chen, Q., Kuwata, M., Ng, N. L., Keutsch, F. N., and Liu, P.: Predicting Real Refractive Index of Organic Aerosols From Elemental Composition, Geophysical Research Letters, 50, e2023GL103446, https://doi.org/10.1029/2023GL103446, e2023GL103446 2023GL103446, 2023.
- Mason, B., Wagner, N. L., Adler, G., Andrews, E., Brock, C. A., Gordon, T. D., Lack, D. A., Perring, A. E., Richardson, M. S., Schwarz, J. P., Shook, M. A., Thornhill, K. L., Ziemba, L. D., and Murphy, D. M.: An intercomparison of aerosol absorption measurements conducted during the SEAC4RS campaign, Aerosol Science and Technology, 52, 1012–1027, https://doi.org/10.1080/02786826.2018.1500012, 2018.
  - McNaughton, C. S., Clarke, A. D., Howell, S. G., Pinkerton, M., Anderson, B., Thornhill, L., Hudgins, C., Winstead, E., Dibb, J. E., Scheuer, E., and Maring, H.: Results from the DC-8 Inlet Characterization Experiment (DICE): Airborne Versus Surface Sampling of Mineral Dust and Sea Salt Aerosols, Aerosol Science and Technology, 41, 136–159, https://doi.org/10.1080/02786820601118406, 2007.
- Mishchenko, M. I. and Travis, L. D.: Capabilities and limitations of a current FORTRAN implementation of the T-matrix method for randomly oriented, rotationally symmetric scatterers, Journal of Quantitative Spectroscopy and Radiative Transfer, 60, 309–324, https://doi.org/10.1016/S0022-4073(98)00008-9, 1998.
  - Moore, R. H., Thornhill, K. L., Weinzierl, B., Sauer, D., D'Ascoli, E., Kim, J., Lichtenstern, M., Scheibe, M., Beaton, B., Beyersdorf, A. J., Barrick, J., Bulzan, D., Corr, C. A., Crosbie, E., Jurkat, T., Martin, R., Riddick, D., Shook, M., Slover, G., Voigt, C., White, R., Winstead, E., Yasky, R., Ziemba, L. D., Brown, A., Schlager, H., and Anderson, B. E.: Biofuel blending reduces particle emissions from aircraft engines at cruise conditions. Nature, 543, 411–415, https://doi.org/10.1038/nature21420, 2017.
- Müller, D., Hostetler, C. A., Ferrare, R. A., Burton, S. P., Chemyakin, E., Kolgotin, A., Hair, J. W., Cook, A. L., Harper, D. B., Rogers, R. R., Hare, R. W., Cleckner, C. S., Obland, M. D., Tomlinson, J., Berg, L. K., and Schmid, B.: Airborne Multiwavelength High Spectral Resolution Lidar (HSRL-2) observations during TCAP 2012: vertical profiles of optical and microphysical properties of a smoke/urban haze plume over the northeastern coast of the US, Atmospheric Measurement Techniques, 7, 3487–3496, https://doi.org/10.5194/amt-7-3487-2014, 2014.

- Nessler, R., Weingartner, E., and Baltensperger, U.: Effect of humidity on aerosol light absorption and its implications for extinction and the single scattering albedo illustrated for a site in the lower free troposphere, Journal of Aerosol Science, 36, 958–972, https://doi.org/10.1016/j.jaerosci.2004.11.012, 2005.
- Painemal, D., Corral, A. F., Sorooshian, A., Brunke, M. A., Chellappan, S., Afzali Gorooh, V., Ham, S.-H., O'Neill, L., Smith Jr., W. L.,

  Tselioudis, G., Wang, H., Zeng, X., and Zuidema, P.: An Overview of Atmospheric Features Over the Western North Atlantic Ocean
  and North American East Coast—Part 2: Circulation, Boundary Layer, and Clouds, Journal of Geophysical Research: Atmospheres, 126,
  https://doi.org/10.1029/2020JD033423, e2020JD033423 2020JD033423, 2021.
  - Petters, M. D. and Kreidenweis, S. M.: A single parameter representation of hygroscopic growth and cloud condensation nucleus activity, Atmospheric Chemistry and Physics, 7, 1961–1971, https://doi.org/10.5194/acp-7-1961-2007, 2007.
- Pistone, K., Redemann, J., Doherty, S., Zuidema, P., Burton, S., Cairns, B., Cochrane, S., Ferrare, R., Flynn, C., Freitag, S., Howell, S. G., Kacenelenbogen, M., LeBlanc, S., Liu, X., Schmidt, K. S., Sedlacek III, A. J., Segal-Rozenhaimer, M., Shinozuka, Y., Stamnes, S., van Diedenhoven, B., Van Harten, G., and Xu, F.: Intercomparison of biomass burning aerosol optical properties from in situ and remotesensing instruments in ORACLES-2016, Atmospheric Chemistry and Physics, 19, 9181–9208, https://doi.org/10.5194/acp-19-9181-2019, 2019.
- Quinn, P., Bates, T., Coffman, D., Upchurch, L., Johnson, J., Moore, R., Ziemba, L., Bell, T., Saltzman, E., Graff, J., and Behrenfeld, M.:

  Seasonal Variations in Western North Atlantic Remote Marine Aerosol Properties, Journal of Geophysical Research: Atmospheres, 124, 14 240–14 261, https://doi.org/10.1029/2019JD031740, 2019.

- Reid, J. S., Jonsson, H. H., Maring, H. B., Smirnov, A., Savoie, D. L., Cliff, S. S., Reid, E. A., Livingston, J. M., Meier, M. M., Dubovik, O., and Tsay, S.-C.: Comparison of size and morphological measurements of coarse mode dust particles from Africa, Journal of Geophysical 1010 Research: Atmospheres, 108, https://doi.org/10.1029/2002JD002485, 2003.
- Reid, J. S., Brooks, B., Crahan, K. K., Hegg, D. A., Eck, T. F., O'Neill, N., de Leeuw, G., Reid, E. A., and Anderson, K. D.: Reconciliation of coarse mode sea-salt aerosol particle size measurements and parameterizations at a subtropical ocean receptor site, Journal of Geophysical Research: Atmospheres, 111, https://doi.org/10.1029/2005JD006200, 2006.
- Reid, J. S., Maring, H. B., Narisma, G. T., van den Heever, S., Girolamo, L. D., Ferrare, R., Lawson, P., Mace, G. G., Simpas, J. B., Tanelli, S., 1015 Ziemba, L., van Diedenhoven, B., Bruinties, R., Bucholtz, A., Cairns, B., Cambaliza, M. O., Chen, G., Diskin, G. S., Flynn, J. H., Hostetler,
- C. A., Holz, R. E., Lang, T. J., Schmidt, K. S., Smith, G., Sorooshian, A., Thompson, E. J., Thornhill, K. L., Trepte, C., Wang, J., Woods, S.,
- Yoon, S., Alexandrov, M., Alvarez, S., Amiot, C. G., Bennett, J. R., Brooks, M., Burton, S. P., Cavanan, E., Chen, H., Collow, A., Crosbie, E., DaSilva, A., DiGangi, J. P., Flagg, D. D., Freeman, S. W., Fu, D., Fukada, E., Hilario, M. R. A., Hong, Y., Hristova-Veleva, S. M., Kuehn, R., Kowch, R. S., Leung, G. R., Loveridge, J., Meyer, K., Miller, R. M., Montes, M. J., Moum, J. N., Nenes, A., Nesbitt, S. W.,
- 1020 Norgren, M., Nowottnick, E. P., Rauber, R. M., Reid, E. A., Rutledge, S., Schlosser, J. S., Sekiyama, T. T., Shook, M. A., Sokolowsky, G. A., Stamnes, S. A., Tanaka, T. Y., Wasilewski, A., Xian, P., Xiao, Q., Xu, Z., and Zavaleta, J.: The Coupling Between Tropical Meteorology, Aerosol Lifecycle, Convection, and Radiation during the Cloud, Aerosol and Monsoon Processes Philippines Experiment
- (CAMP2Ex), Bulletin of the American Meteorological Society, 104, E1179 E1205, https://doi.org/10.1175/BAMS-D-21-0285.1, 2023. Rolph, G., Stein, A., and Stunder, B.: Real-time Environmental Applications and Display system; READY, Environmental Modelling & 1025

Software, 95, 210–228, https://doi.org/10.1016/j.envsoft.2017.06.025, 2017.

- Ryder, C. L., McQuaid, J. B., Flamant, C., Rosenberg, P. D., Washington, R., Brindley, H. E., Highwood, E. J., Marsham, J. H., Parker, D. J., Todd, M. C., Banks, J. R., Brooke, J. K., Engelstaedter, S., Estelles, V., Formenti, P., Garcia-Carreras, L., Kocha, C., Marenco, F., Sodemann, H., Allen, C. J. T., Bourdon, A., Bart, M., Cavazos-Guerra, C., Chevaillier, S., Crosier, J., Darbyshire, E., Dean, A. R., Dorsey, J. R., Kent, J., O'Sullivan, D., Schepanski, K., Szpek, K., Trembath, J., and Woolley, A.: Advances in understanding mineral dust 1030 and boundary layer processes over the Sahara from Fennec aircraft observations, Atmospheric Chemistry and Physics, 15, 8479-8520, https://doi.org/10.5194/acp-15-8479-2015, 2015.
  - Ryder, C. L., Marenco, F., Brooke, J. K., Estelles, V., Cotton, R., Formenti, P., McQuaid, J. B., Price, H. C., Liu, D., Ausset, P., Rosenberg, P. D., Taylor, J. W., Choularton, T., Bower, K., Coe, H., Gallagher, M., Crosier, J., Lloyd, G., Highwood, E. J., and Murray, B. J.: Coarsemode mineral dust size distributions, composition and optical properties from AER-D aircraft measurements over the tropical eastern Atlantic, Atmospheric Chemistry and Physics, 18, 17 225-17 257, https://doi.org/10.5194/acp-18-17225-2018, 2018.
  - Sawamura, P., Moore, R. H., Burton, S. P., Chemyakin, E., Müller, D., Kolgotin, A., Ferrare, R. A., Hostetler, C. A., Ziemba, L. D., Beversdorf, A. J., and Anderson, B. E.: HSRL-2 aerosol optical measurements and microphysical retrievals vs. airborne in situ measurements during DISCOVER-AQ 2013: an intercomparison study, Atmospheric Chemistry and Physics, 17, 7229–7243, https://doi.org/10.5194/acp-17-7229-2017, 2017.
- 1046 Schlosser, J. S., Stamnes, S., Burton, S. P., Cairns, B., Crosbie, E., Van Diedenhoven, B., Diskin, G., Dmitrovic, S., Ferrare, R., Hair, J. W., Hostetler, C. A., Hu, Y., Liu, X., Moore, R. H., Shingler, T., Shook, M. A., Thornhill, K. L., Winstead, E., Ziemba, L., and Sorooshian, A.: Polarimeter + Lidar-Derived Aerosol Particle Number Concentration, Frontiers in Remote Sensing, 3, https://doi.org/10.3389/frsen.2022.885332, 2022.

- Schlosser, J. S., Bennett, R., Cairns, B., Chen, G., Collister, B. L., Hair, J. W., Jones, M., Shook, M. A., Sorooshian, A., Thornhill, K. L.,

  Ziemba, L. D., and Stamnes, S.: Maximizing the Volume of Collocated Data from Two Coordinated Suborbital Platforms, Journal of Atmospheric and Oceanic Technology, 41, 189 201, https://doi.org/10.1175/JTECH-D-23-0001.1, 2024.
- Schroeder, W., Oliva, P., Giglio, L., and Csiszar, I. A.: The New VIIRS 375m active fire detection data product: Algorithm description and initial assessment, Remote Sensing of Environment, 143, 85–96, https://doi.org/10.1016/j.rse.2013.12.008, 2014.
- Shingler, T., Dey, S., Sorooshian, A., Brechtel, F. J., Wang, Z., Metcalf, A., Coggon, M., Mülmenstädt, J., Russell, L. M., Jonsson, H. H., and Seinfeld, J. H.: Characterisation and airborne deployment of a new counterflow virtual impactor inlet, Atmospheric Measurement Techniques, 5, 1259–1269, https://doi.org/10.5194/amt-5-1259-2012, 2012.

1070

e2019JD031626 2019JD031626, 2020.

- Shingler, T., Sorooshian, A., Ortega, A., Crosbie, E., Wonaschütz, A., Perring, A. E., Beyersdorf, A., Ziemba, L., Jimenez, J. L., Campuzano-Jost, P., Mikoviny, T., Wisthaler, A., and Russell, L. M.: Ambient observations of hygroscopic growth factor and f(RH) below 1: Case studies from surface and airborne measurements, Journal of Geophysical Research: Atmospheres, 121, 13,661–13,677, https://doi.org/10.1002/2016JD025471, 2016.
- Sinclair, K., van Diedenhoven, B., Cairns, B., Alexandrov, M., Moore, R., Crosbie, E., and Ziemba, L.: Polarimetric retrievals of cloud droplet number concentrations, Remote Sensing of Environment, 228, 227–240, https://doi.org/10.1016/j.rse.2019.04.008, 2019.
- Soloff, C., Ajayi, T., Choi, Y., Crosbie, E. C., DiGangi, J. P., Diskin, G. S., Fenn, M. A., Ferrare, R. A., Gallo, F., Hair, J. W., Hilario, M. R. A., Kirschler, S., Moore, R. H., Shingler, T. J., Shook, M. A., Thornhill, K. L., Voigt, C., Winstead, E. L., Ziemba, L. D., and Sorooshian, A.: Bridging Gas and Aerosol Properties between Northeast U.S. and Bermuda: Analysis of Eight Transit Flights, EGUsphere, 2024, 1–41,
- Bridging Gas and Aerosol Properties between Northeast U.S. and Bermuda: Analysis of Eight Transit Flights, EGUsphere, 2024, 1–41, https://doi.org/10.5194/egusphere-2024-926, 2024.
  - Sorooshian, A., Anderson, B., Bauer, S. E., Braun, R. A., Cairns, B., Crosbie, E., Dadashazar, H., Diskin, G., Ferrare, R., Flagan, R. C., Hair, J., Hostetler, C., Jonsson, H. H., Kleb, M. M., Liu, H., MacDonald, A. B., McComiskey, A., Moore, R., Painemal, D., Russell, L. M., Seinfeld, J. H., Shook, M., Smith, W. L., Thornhill, K., Tselioudis, G., Wang, H., Zeng, X., Zhang, B., Ziemba, L., and Zuidema, P.:
- Aerosol-Cloud-Meteorology Interaction Airborne Field Investigations: Using Lessons Learned from the U.S. West Coast in the Design of ACTIVATE off the U.S. East Coast, Bulletin of the American Meteorological Society, 100, 1511 1528, https://doi.org/10.1175/BAMS-D-18-0100.1, 2019.
  - Sorooshian, A., Corral, A. F., Braun, R. A., Cairns, B., Crosbie, E., Ferrare, R., Hair, J., Kleb, M. M., Hossein Mardi, A., Maring, H., Mc-Comiskey, A., Moore, R., Painemal, D., Scarino, A. J., Schlosser, J., Shingler, T., Shook, M., Wang, H., Zeng, X., Ziemba, L., and Zuidema, P.: Atmospheric Research Over the Western North Atlantic Ocean Region and North American East Coast: A Review of Past Work and Challenges Ahead, Journal of Geophysical Research: Atmospheres, 125, e2019JD031626, https://doi.org/10.1029/2019JD031626,
  - Sorooshian, A., Alexandrov, M. D., Bell, A. D., Bennett, R., Betito, G., Burton, S. P., Buzanowicz, M. E., Cairns, B., Chemyakin, E. V., Chen, G., Choi, Y., Collister, B. L., Cook, A. L., Corral, A. F., Crosbie, E. C., van Diedenhoven, B., DiGangi, J. P., Diskin, G. S., Dmitrovic,
- S., Edwards, E.-L., Fenn, M. A., Ferrare, R. A., van Gilst, D., Hair, J. W., Harper, D. B., Hilario, M. R. A., Hostetler, C. A., Jester, N., Jones, M., Kirschler, S., Kleb, M. M., Kusterer, J. M., Leavor, S., Lee, J. W., Liu, H., McCauley, K., Moore, R. H., Nied, J., Notari, A., Nowak, J. B., Painemal, D., Phillips, K. E., Robinson, C. E., Scarino, A. J., Schlosser, J. S., Seaman, S. T., Seethala, C., Shingler, T. J., Shook, M. A., Sinclair, K. A., Smith Jr., W. L., Spangenberg, D. A., Stamnes, S. A., Thornhill, K. L., Voigt, C., Vömel, H., Wasilewski, A. P., Wang, H., Winstead, E. L., Zeider, K., Zeng, X., Zhang, B., Ziemba, L. D., and Zuidema, P.: Spatially coordinated airborne data and
- 1080 complementary products for aerosol, gas, cloud, and meteorological studies: the NASA ACTIVATE dataset, Earth System Science Data, 15, 3419–3472, https://doi.org/10.5194/essd-15-3419-2023, 2023.

- Sorribas, M., Olmo, F. J., Quirantes, A., Lyamani, H., Gil-Ojeda, M., Alados-Arboledas, L., and Horvath, H.: Role of spheroidal particles in closure studies for aerosol microphysical–optical properties, Quarterly Journal of the Royal Meteorological Society, 141, 2700–2707, https://doi.org/10.1002/qi.2557, 2015.
- Stamnes, S., Hostetler, C., Ferrare, R., Burton, S., Liu, X., Hair, J., Hu, Y., Wasilewski, A., Martin, W., van Diedenhoven, B., et al.: Simultaneous polarimeter retrievals of microphysical aerosol and ocean color parameters from the "MAPP" algorithm with comparison to high-spectral-resolution lidar aerosol and ocean products, Applied Optics, 57, 2394–2413, https://doi.org/10.1364/AO.57.002394, 2018.

- Stein, A. F., Draxler, R. R., Rolph, G. D., Stunder, B. J. B., Cohen, M. D., and Ngan, F.: NOAA's HYSPLIT Atmospheric Transport and Dispersion Modeling System, Bulletin of the American Meteorological Society, 96, 2059 2077, https://doi.org/10.1175/BAMS-D-14-00110.1, 2015.
- Tsekeri, A., Amiridis, V., Marenco, F., Nenes, A., Marinou, E., Solomos, S., Rosenberg, P., Trembath, J., Nott, G. J., Allan, J., Le Breton, M., Bacak, A., Coe, H., Percival, C., and Mihalopoulos, N.: Profiling aerosol optical, microphysical and hygroscopic properties in ambient conditions by combining in situ and remote sensing, Atmospheric Measurement Techniques, 10, 83–107, https://doi.org/10.5194/amt-10-83-2017, 2017.
- van Diedenhoven, B., Hasekamp, O. P., Cairns, B., Schuster, G. L., Stamnes, S., Shook, M., and Ziemba, L.: Remote sensing of aerosol water fraction, dry size distribution and soluble fraction using multi-angle, multi-spectral polarimetry, Atmospheric Measurement Techniques, 15, 7411–7434, https://doi.org/10.5194/amt-15-7411-2022, 2022.
- Veselovskii, I., Dubovik, O., Kolgotin, A., Lapyonok, T., Di Girolamo, P., Summa, D., Whiteman, D. N., Mishchenko, M., and Tanré, D.:

  Application of randomly oriented spheroids for retrieval of dust particle parameters from multiwavelength lidar measurements, Journal of

  Geophysical Research: Atmospheres, 115, <a href="https://doi.org/10.1029/2010JD014139">https://doi.org/10.1029/2010JD014139</a>, 2010.
  - Virkkula, A.: Correction of the Calibration of the 3-wavelength Particle Soot Absorption Photometer ( $3\lambda$  PSAP), Aerosol Science and Technology, 44, 706–712, https://doi.org/10.1080/02786826.2010.482110, 2010.
- Voshchinnikov, N. V. and Farafonov, V. G.: Optical properties of spheroidal particles, Astrophysics and Space Science, 204, 19–86, https://doi.org/10.1007/BF00658095, 1993.
- Wagner, R., Ajtai, T., Kandler, K., Lieke, K., Linke, C., Müller, T., Schnaiter, M., and Vragel, M.: Complex refractive indices of Saharan dust samples at visible and near UV wavelengths: a laboratory study, Atmospheric Chemistry and Physics, 12, 2491–2512, https://doi.org/10.5194/acp-12-2491-2012, 2012.
  - Wu, L., Hasekamp, O., van Diedenhoven, B., and Cairns, B.: Aerosol retrieval from multiangle, multispectral photopolarimetric measurements: importance of spectral range and angular resolution, Atmospheric Measurement Techniques, 8, 2625–2638, https://doi.org/10.5194/amt-8-2625-2015, 2015.
  - Zieger, P., Fierz-Schmidhauser, R., Weingartner, E., and Baltensperger, U.: Effects of relative humidity on aerosol light scattering: results from different European sites, Atmospheric Chemistry and Physics, 13, 10609–10631, https://doi.org/10.5194/acp-13-10609-2013, 2013.
- Ziemba, L. D., Lee Thornhill, K., Ferrare, R., Barrick, J., Beyersdorf, A. J., Chen, G., Crumeyrolle, S. N., Hair, J., Hostetler, C., Hudgins, C., Obland, M., Rogers, R., Scarino, A. J., Winstead, E. L., and Anderson, B. E.: Airborne observations of aerosol extinction by in situ and remote-sensing techniques: Evaluation of particle hygroscopicity, Geophysical Research Letters, 40, 417–422, https://doi.org/10.1029/2012GL054428, 2013.